CZECH TECHNICAL UNIVERSITY IN PRAGUE

FACULTY OF NUCLEAR SCIENCES AND PHYSICAL ENGINEERING

Department of Physics

Physics and Technology of Nuclear Fusion

RESEARCH PROJECT

Proposal of X rays and gamma detector for experiments on laser-driven ion acceleration

Návrh detektoru rentgenového a gama záření pro experimenty s laserovým urychlováním iontů

Author: Bc. Valeriia Istokskaia
Supervisor: Lorenzo Giuffrida, Ph.D.
Consultants: Ing. Jan Pšikal, Ph.D.
Roberto Versaci, Ph.D.

Prague, 2018

Prohlášení

Prohlašuji, že jsem svou bakalářskou práci vypracovala samostatně a použila jsem pouze podklady (literaturu, projekty, SW atd.) uvedené v přiloženém seznamu.

Nemám závažný důvod proti použití tohoto školního díla ve smyslu §60 Zákona č. 121/2000 Sb., o právu autorském, o právech souvisejících s právem autorským a o změně některých zákonů (autorský zákon).

V Praze dne .....

.....
Bc. Valeriia Istokskaia

Acknowlegement

I would like to express my sincere gratitude to my supervisor Lorenzo Giuffrida, Ph.D. for his guidance, patience and encouragement throughout the work. Furthemore, I would like to thank my consultants Roberto Vercaci, Ph.D. and Ing. Jan Pšikal, Ph.D. for providing me with invaluably constructive criticism and useful suggestions. I am also very grateful to Ing. Vojtěch Stránský for his friendly approach while introducing me to the topic.

Bc. Valeriia Istokskaia

Název práce: **Návrh detektoru rentgenového a gama záření pro experimenty s laserovým urychlováním iontů**

Autor: Bc. Valeriia Istokskaia
Obor: Fyzika a Technika Termojaderné Fúze
Druh práce: Výzkumný úkol
Vedoucí práce: Lorenzo Giuffrida, Ph.D., FZÚ AV ČR
Konzultanty: Ing. Jan Pšikal, Ph.D., KFE FJFI ČVUT
Roberto Versaci, Ph.D., FZÚ AV ČR

Abstrakt: Tato práce má za cíl navrhnout nový typ detektoru rentgenového a gama záření pro nadcházející experimenty ve výzkumném centru ELI Beamlines. Vzhledem k tomu, že lasery v ELI Beamlines budou charakterizovány ultravysokými výkony a intenzitami (více než 10^{21} W/cm^2), extrémně intenzivní a krátké pulsy energetických fotonů (rtg a gama s teplotou až 50 MeV) budou vyzařovány během interakce těchto laserů s terči. Běžně používaná diagnostika není schopná provádět spektrometrii pulzního fotonového záření, a proto je vyvíjen nový online detektor – elektromagnetický kalorimetr. V ideálním případě takový detektor bude schopen odhadnout teplotu produkovaných fotonů. Táto práce zahrnuje popis výsledků simulací, které byly provedené pro návrh kalorimetru pomocí simulačního kódu FLUKA, a možný algoritmus rekonstrukce signálu z detektoru.

Klíčová slova: detektor gama záření, elektromagnetický kalorimetr, rentgenové záření, urychlování laserem, fyzika plazmatu

Title of work: **Proposal of X rays and gamma detector for experiments on laser-driven ion acceleration**

Author: Bc. Valeriia Istokskaia
Specialization: Physics and Technology of Nuclear Fusion
Type of thesis: Research project
Supervisor: Lorenzo Giuffrida, Ph.D., FZÚ AV ČR
Consultants: Ing. Jan Pšikal, Ph.D., KFE FJFI ČVUT
Roberto Versaci, Ph.D., FZÚ AV ČR

Abstract: The thesis aims to propose a new type of gamma detector for upcoming experiments in the frame of ELI Beamlines project. Since lasers with ultra-high peak powers and intensities (more than 10^{21} W/cm^2) will be available at ELI Beamlines, extremely intense and short high-energy photon bursts (up to 50 MeV) will be emitted during the laser-matter interaction. The currently used diagnostics is not suitable for spectroscopy of such radiation, therefore a novel online detector, an electromagnetic calorimeter, is being developed. Ideally, such detector should be capable to estimate the temperature of the generated photons. The thesis describes the simulations that were performed employing the Monte Carlo FLUKA code to design the calorimeter and the event reconstruction techniques studied.

Key words: gamma detector, electromagnetic calorimeter, X rays, laser acceleration, plasma physics

Contents

Introduction

With the advent of laser technology in the last century, it became possible to use lasers for plasma production and subsequently for plasma acceleration. Nowadays, ions with the energy of several tens of MeV/nukleon can be accelerated by using a laser with high intensity and short pulse duration [1].

One of the research groups studying laser-driven ion acceleration is the ELIMAIA (ELI Multidisciplinary Applications of laser-Ion Acceleration) group from ELI Beamlines facility (Extreme Light Infrastructure) in Prague. Since lasers with ultra-high peak powers and intensities more than 10^{21} W/cm^2 will be available in ELI Beamlines, during the laser-target interaction the production of accelerated ions will be accompanied by very intensive and short high-energy photon bursts (gamma and X-rays with temperatures up to 50 MeV). Spectroscopy of the photon emission can provide with information about generated charged particles energies and physics of the acceleration process. However, the currently used diagnostics is not suitable for spectroscopy of such radiation. Therefore, a novel electromagnetic calorimeter capable of the photon temperature estimation is being developed in collaboration between ELIMAIA and Monte-Carlo groups from ELI Beamlines.

The first chapter of the thesis summarizes the theory of laser-plasma interaction and particle acceleration mechanisms. The second one describes the physics of X-rays and gamma-rays generation and principles of their interaction with matter. Chapter 3 aims to give an overview of some of the most common photon diagnostics used nowadays, including gaseous, solid-state detectors and electromagnetic calorimeters and discusses their benefits and drawbacks. The final chapter summarizes the current progress of the developed calorimeter, based on simulations performed using the Monte Carlo FLUKA code, including estimation of plasma-emitted photons temperature, the description of possible designs, materials and a signal unfolding algorithm.

Chapter 1

Theory of laser-plasma interaction and ion acceleration

Laser-plasma interaction is an exciting discipline of modern Physics that has been explored since the realization of the first laser in 1960 [2]. Later on, in 1979, Tajima and Dawson first proposed the idea of using laser-plasma interactions to accelerate charged particles [3]. Their paper describes the principle of laser-electron acceleration in a so called electrostatic wake field, that is formed behind the laser pulse as it penetrates through the underdense plasma. However, it became apparent soon, that the laser intensity should be increased to achieve higher kinetic energies of accelerated particles. Long pulsed lasers appeared to be too expensive for that purpose, so the focus was set on shorter laser pulse systems (picoseconds or subpicosecond regime), that were relatively small and cheap. The invention of the chirped pulse amplification (CPA) technique has enabled to obtain ultra-short, ultra-high intensity pulses with typical duration in terms of femtoseconds, avoiding problem of destroying an amplifier medium [4],[5].

Since then, a lot of innovations have been developed leading to a tremendous progress in laser technology. Nowadays, high power laser-matter interaction means lasers with intensities ranging from 10^{10} W/cm^2 to approximately 10^{22} W/cm^2 delivering energy to a target over nanoseconds down to few femtoseconds time ranges [6]. For instance, the worlds most intense laser system with ultra-high peak powers of 10 PW and focused intensities up to 10^{24} W/cm^2 will soon be available at ELI Beamlines (Extreme Light Infrastructure) center in Prague [7].

Focused on a target, such lasers induce a rapid ionization near the target surface and subsequent matter transformation into a dense plasma. This process happens since the electric field of the high-power laser pulse is much stronger than the Coulomb field that bind electrons and atomic nuclei. The fundamental properties of the created plasma depend on both target and laser radiation parameters. Basic plasma characteristics and principles of laser pulse propagation and absorption in plasma will be discussed in this chapter, along with the most common laser acceleration mechanisms.

1.1 Basic characteristics of plasma

Plasma is a *quasineutral* gas of charged and neutral particles which exhibits *collective behavior* [8].

The latter term means that particle motions in a plasma depend not only on local conditions but also on the state of the plasma in distant regions. This indicates, that the influence of macroscopic electromagnetic fields on the particle interactions prevails over microscopic fields occurring in binary collisions.

The concept of quasineutrality lays in the fact that the total plasma charge is much lower than the total positive charge. The plasma appears quasineutral at time scales much larger than the reciprocal plasma frequency (Eq. 1.7) and at spatial scales much larger than the Debye length (Eq. 1.2). Assuming that n_e, n_i denote respectively electron and ion densities and Z is the average charge of ions, the condition of quasineutrality can be expressed as

$$n_e \cong Z n_i \cong n, \tag{1.1}$$

where n is referred to as *plasma density*.

Charge fluctuations in plasma are compensated at the dimensions much larger than a Debye length distance. This is the result of a phenomenon called *Debye shielding*, which is a fundamental property of a plasma indicating its ability to shield (screen) intrinsic electric potentials. The shielding is implemented by the slight displacement of charged plasma particles so as to reduce the effectiveness of the arisen field. Given that a "test" particle carrying non-zero charge is placed into the initially unperturbed plasma, opposite charges present in the medium start to be attracted to it, forming a cloud surrounding the primal particle. Shielding distance or thickness of such a charged cloud is called the Debye length and is defined as [8]

$$\lambda_D = \sqrt{\frac{\varepsilon_0 k_B T}{n_e e^2}}, \tag{1.2}$$

where T is the temperature in K, k_B is the Bolzmann constant in J/K, n_e is electron density in m^{-3}, e is electron charge in C and ε_0 is dielectric constant (F/m). For example, for temperature T = 1 keV = 11600×10^3 K and electron density of 10^{21} m^{-3} the Debye length is $\lambda_D = 0.2$ μm.

Apparently, the Debye length definition is only valid if the number of particles in the plasma is high enough to establish an effective shield. A criterion for the determination of the sufficient amount of particles is called Plasma parameter and is calculated as the particles number in a Debye sphere (presuming λ_D is the sphere's radius - Fig.1.1) [8]:

$$N_D = n_e \frac{4}{3}\pi\lambda_D^3 \simeq 1.36 \times 10^6 \; T^{\frac{3}{2}} n_e^{-\frac{1}{2}}. \tag{1.3}$$

So, for successful electric potentials screening, the plasma parameter ought to satisfy the following condition:

$$N_D \gg 1. \tag{1.4}$$

Due to the fact, that the mass of electrons is more than 1000 times smaller than that of any ion, they appear to be more mobile and move faster. Moving so as to surround an excess of positive charge or repulse from the excess of negative charge they mainly accomplish the Debye shielding. The eventual electric potential $\phi(r)$ in the plasma, depending on the distance r from the test particle, can be calculated according to the following equation [9]:

$$\phi(r) = \phi_0 \exp(-\frac{r}{\lambda_D}). \tag{1.5}$$

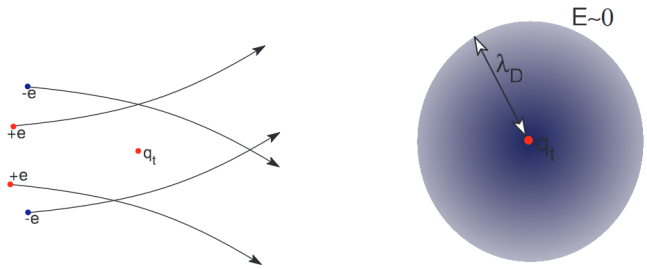

Fig. 1.1. Sketch of the particle trajectories and charge distribution in the Debye sphere in the vicinity of a test charge q_t. [9].

For $r \ll \lambda_D$ the potential $\phi(r)$ is identical to the Coulomb potential $\phi_0 = \frac{e}{4\pi\epsilon_0 r}$ of a test particle in vacuum, whereas for $r \gg \lambda_D$ the test charge is completely screened by its surrounding shielding cloud. So, it is clearly seen, than in the plasma, in comparison to vacuum, the potential is exponentially damped with the strength of damping given by the Debye length. This imposes the next condition on the plasma, that demands the plasma size L precedes the Debye length:

$$L \gg \lambda_D. \tag{1.6}$$

A very important parameter in the view of the plasma collective behavior is the plasma (Langmuir) frequency. It is depicted as the oscillation frequency of an electron layer about its initial position. If some electromagnetic wave, e.g. laser pulse, interacts with the plasma, electrons are slightly dislocated from their initial positions while ions are almost at rest due to their larger mass. This charge separation is responsible for a restoring force as it generates uniform electric field. Consequently, the plasma is subjected to oscillations with frequency [8]:

$$\omega_p = \sqrt{\frac{n_e e^2}{m_e \varepsilon_0}}. \tag{1.7}$$

If the condition 1.8 is satisfied, where ν_c is the frequency of binary collisions, than collective motion in the plasma prevails over binary interactions.

$$\omega_p \gg \nu_c. \tag{1.8}$$

1.2 Propagation and absorption of laser wave in plasma

1.2.1 Propagation

A laser pulse is basically an electromagnetic wave. A dispersion relation of the electromagnetic wave propagating in plasma is [10]

$$\omega^2 = \omega_p^2 + c^2 k^2 \tag{1.9}$$

where k is the wave vector, ω denotes the frequency of electromagnetic (EM) wave (laser frequency) and ω_p the plasma frequency 1.7.

Depending on the frequency ω of the laser wave, 3 cases may take place:

- $\omega > \omega_p, k$ is real and the wave propagates through the plasma. It happens since the electrons are not able to follow the field oscillations because of their own inertia, thus the plasma acts as a transparent media for the laser wave. Such a plasma is called *underdense plasma*.

- $\omega < \omega_p, k$ is imaginary and the wave is exponentially damped. It propagates into the plasma only until a finite depth - the collisionless skin depth $l_s = \frac{c}{\omega_p}$. In this situation the plasma is called *overdense*.

- $\omega \simeq \omega_p, k \simeq 0$, the wave is reflected, as electrons the oscillating in the laser field impede its propagation. The electron density corresponding to the laser wave reflection is called *critical density* and is calculated as [11]

$$n_{cr} = \frac{\varepsilon_0 m_e}{e^2}\omega^2 = 1.1 \times 10^{15} m^{-3} \left(\frac{\lambda}{1\mu m}\right)^{-2} \tag{1.10}$$

  So, the critical density distinguishes between the underdense and the overdense plasma regimes.

The motion of charged particles in the electromagnetic field is governed by the Lorentz force:

$$\vec{F_l} = q\left(\vec{E} + \vec{v} \times \vec{B}\right), \tag{1.11}$$

where $\vec{B}$ denotes the magnetic field, $\vec{E}$ is the electric field, $\vec{v}$ is the velocity and q is the charge of a particle.

Furthermore, electrons in the relativistic laser fields experience a non-linear force which is caused by the electric field inhomogenuity called the ponderomotive force.This force tends to push the electron against the gradient of slowly-varying averaged laser electric field until the ponderomotive potential Φ_{pon} is compensated by the electrostatic potential Φ_{el} between the replaced electrons and ions. Ponderomotive force can be expressed as [12]

$$F_{pon} = -m_e c^2 \nabla\langle\gamma\rangle = -\frac{e^2}{4m_e\omega^2}\nabla\langle\vec{E}^2\rangle \tag{1.12}$$

where $\langle\gamma\rangle$ denotes relativistic factor averaged over the fast laser field oscillations and $\langle\vec{E}^2\rangle$ is averaged laser electric field.

A parameter which determines whether the electron motion should be treated as relativistic or not is the dimensionless amplitude a_0 of the vector potential $\vec{A}$ in the Coulomb gauge [13]

$$a_0 = \frac{eE_0}{m_e\omega c}, \tag{1.13}$$

where ω stands for the angular frequency of the electromagnetic wave and E_0 is the strength of the electric field. If $a_0 \ll 1$, the case is non-relativistic. On the other hand, $a_0 \geq 1$ indicates that electrons oscillate with a relativistic velocity.

Using the dimensionless amplitude, the laser irradiance can be defined as

$$I_L \lambda_L = a_0^2 \times 1.37 \times 10^{18}, \tag{1.14}$$

where I_L is the intensity of the laser wave and λ_L is the laser wavelength. According to the latter equation, relativistic regime starts to prevail above 10^{18} W/cm^2.

1.2.2 Absorption

The absorption mechanism of electromagnetic radiation is a process in which the energy of a photon is transferred to the matter the electromagnetic wave interacts with.

Laser light on the short time scales interacts mainly with electrons, due to their high mobility, hence laser radiation energy is transferred to a plasma via electrons which then pass it to ions.

Absorption of the laser light by the plasma electrons can proceed either by collisions with nucleus or through collisionless mechanisms. Which process dominates in the plasma depends strongly on the incident laser intensity. As it was mentioned in the previous section, the magnitude of the laser intensity influences electron motion, resulting in the electron velocities being relativistic or not.

For laser intensities lower than 10^{16} W/cm^2, absorption will mainly occur through collisions. *Inverse Bremsstrahlung* mechanism is an example of collisional absorption: electron gains its kinetic energy from oscillating laser wave and is subsequently thermalized by collisions with a nucleus [14].

However, with the increase of electrons energy, the collisional frequency between ions and electrons ν_c decreases, as it is in inverse ratio to the electron velocity v_e [12]:

$$\nu_{ei} = \frac{3Z^2 e^4 n_i \ln \Lambda}{8\pi \epsilon^2 m_e^2 v_e^3}, \tag{1.15}$$

where $\ln \Lambda$ is the Coulomb logarithm and Z is the ion charge number.

For higher laser intensities collisional absorption becomes negligible in comparison to other absorption mechanisms that start to prevail. These mechanisms are called collisionless and are briefly described in the following text.

- **Resonance absorption**

This mechanism lies in resonant excitation of an electron plasma wave which then propagates into the overdense plasma.

Intense laser pulses are frequently preceded by a less intense prepulse, that may cause pre-expansion of the target and subsequent formation of a relatively small density gradient. The resonance takes place in a region of the plasma density, where the plasma frequency ω_p is equal to the laser frequency ω.

If the laser wave is obliquely incident on the target at some angle θ, it will propagate only up to the density named turning point, where it is reflected (Fig.1.2). The turning point is shifted from the critical density towards lower densities [15]:

$$n_{turn} = n_{cr} \cos^2 \theta \tag{1.16}$$

However, if the wave is p-polarized, some of its energy tunnels up to the critical density surface. It happens since the electric field $\vec{E}$ of such a wave lies in the direction

of the density gradient. Therefore it can resonantly excite electron plasma (Langmuir) wave in the critical layer by separating positive and negative charges.

On the contrary, in the case of s-polarized wave no resonance, and hence energy transfer, is achievable. In this case, the directions of the laser electric field and the plasma density gradient no longer coincide, as the electric field vector is now perpendicular to the incidence plane. Illustration of both cases is presented in Fig. 1.2.

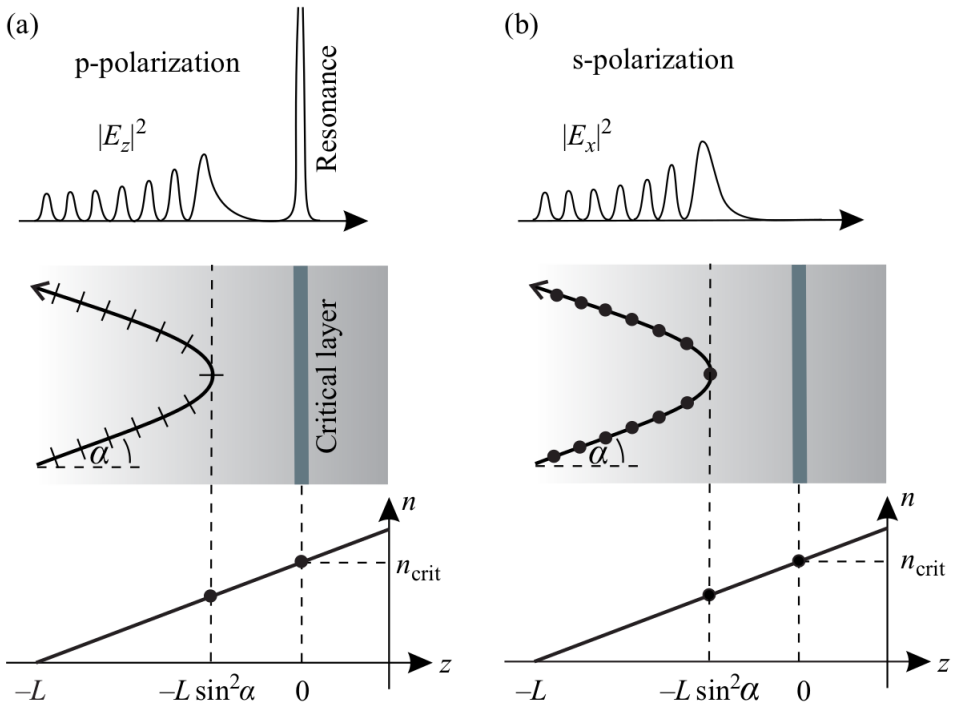

Fig. 1.2. Sketch of the resonance absorption mechanism for a) p-polarized laser and b) s-polarized laser wave [16].

- **Vacuum Heating**

This type of absorption occurs in high intensity laser-plasma interaction when steep density gradients are considered. As this mechanism was firstly described by Brunel in 1987 [17], it is also known as *Brunel heating*.

In this scenario, a p-polarized laser wave is obliquely incident on the plasma with a steep density gradient and the electron oscillation amplitude exceeds its scale length. Electrons in the plasma-vacuum boundary are pulled out from the target to the vacuum under the influence of the laser pulse electric field. When the field changes its direction during later phase of one cycle of the laser wave, accelerated electrons are injected back in the plasma. Since the laser field is attenuated in the overdense plasma, electrons can propagate further uninfluenced, and a part of the laser energy they carry is completely scattered in the plasma. Stages of this process are depicted on Fig.1.3.

- $\vec{\mathbf{j}} \times \vec{\mathbf{B}}$ **heating**

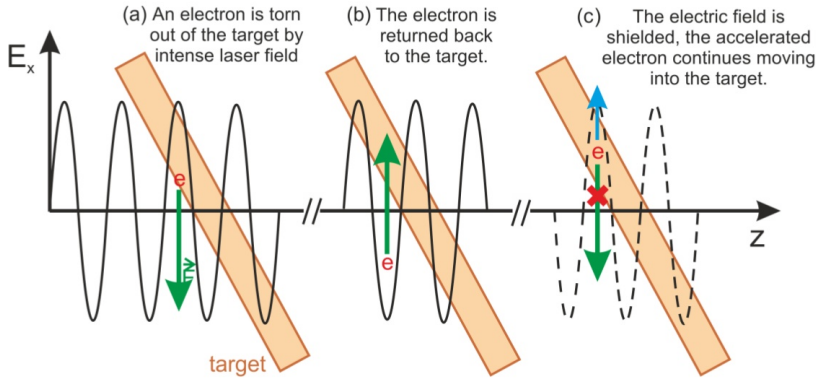

Fig. 1.3. Stages of Brunel heating process [18].

Similar to Brunel heating, $\vec{j} \times \vec{B}$ mechanism also requires a very steep density gradient. The difference is that in this process electrons motion is treated as relativistic and hence the magnetic component of the Lorenz force (Eq. 1.11) becomes significant, whilst in the vacuum heating electrons were driven only by the electric field. Thus, electrons are extracted into vacuum twice during the laser period by combination of the electric and the magnetic field, whereas in Brunel heating only once.

The advantage of this mechanism is that due to the magnetic component it can be efficient even for perpendicular incidence of the laser pulse and for s-polarized wave.

1.3 Laser-driven ion acceleration mechanisms

Nowadays laser-driven particle acceleration in plasma is a promising candidate for replacing conventional large acceleration systems such as cyclotron or synchrotron. These accelerators are used for different purposes in various areas from nuclear physics to tumor treatment, and their history counts more than 70 years of developing and enhancement [19]. However, each cyclotron or synchrotron has definite break down limit. To overcome it and to reach higher energies, rebuilding towards bigger size of construction is required, which is impractical from economical points of view.

On the contrary, laser-driven accelerators are compact, as they are able to accelerate particles up to energies of tens of MeV over only a few micrometer distances, having shorter pulse duration [20]. Also there is no break down limit for the maximum energy in comparison to conventional ones. Moreover, any kind of charged particle can be accelerated with the help of one and the same laser-driven accelerator. The reason is, that a particle source in this case is represented by a target, whose compound can be easily changed with respect to required ions.

Active research in this field is ongoing throughout the world. For instance, laser-driven ion acceleration is examined at ELI Beamlines center in the Czech Republic by ELIMAIA group (ELI Multidisciplinary Applications of laser-Ion Acceleration). The main purpose of this group is to ensure stable, fully characterized and tunable ion beams accelerated by Petawatt-class lasers for the use in multidisciplinary applications (radiobiology, hadrohterapy, etc) [21].

Although laser-driven accelerators possess undisputed advantages, there are some limitations to be overcome. For instance, achieving monoenergetic particle beam and high repetition rate are required to let laser-driven accelerators be competitive with conventional ones in the manner of beams quality.

Depending on target thickness and laser properties (pulse duration, laser power), different ion acceleration mechanisms can occur. Two main regimes, Target Normal Sheath Acceleration (TNSA) and Radiation Pressure Acceleration (RPA), that were studied theoretically and experimentally over the past two decades [22], [23], will be briefly described in the following sections. Fig.1.4 shows the comparison of these mechanisms with another acceleration regimes depending on the laser intensity and pulse duration.

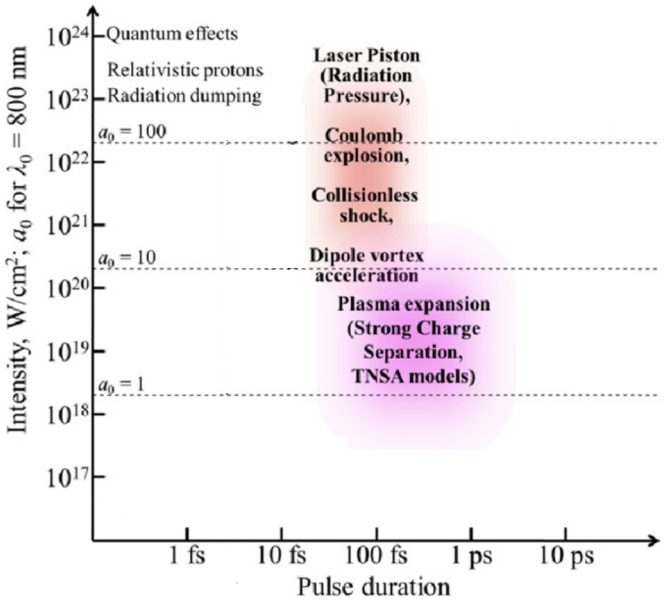

Fig. 1.4. Different regimes of laser ion acceleration in plasma depending on the laser intensity and pulse duration, including TNSA and RPA are sketched in this section. The regimes have no abrupt borders and can overlap one another. In this graph electron density $n_e = 460 n_{cr}$ is assumed in a fully ionized carbon for $\lambda_0 = 800$ nm. ([13], modified).

1.3.1 Target Normal Sheath Acceleration (TNSA)

The principle of TNSA was firstly suggested by Wilks et al. in 2001[24] and now it has become the most experimentally investigated and widely used mechanism of ion acceleration.

A laser pulse irradiating the target transfers its energy into hot electrons, which then penetrate through the target. Targets are usually foils in the micrometer thickness range [11]. Once the hot electrons reach the target rear surface they create a Debye sheath (with the scale of the Debye length). Charge separation results in formation of a strong electric field at the target rear that instantly ionizes atoms. Subsequently,

the ions start to expand into vacuum in the sheath field following the electrons, mainly in the target normal direction. Most of the electrons, however, are pulled back to the foil, as their energy is not high enough to escape their self-induced field. They continue transferring their kinetic energy to the ions by recirculation in the foil. Some of them reach the front target surface and generate a sheath field accelerating the ions in the opposite direction. As the number of electrons outside the foil remains almost constant, equilibrium is established. The ion acceleration continues as long as the laser keeps heating the electrons. A simplified scheme of the TNSA is shown in Fig.1.5.

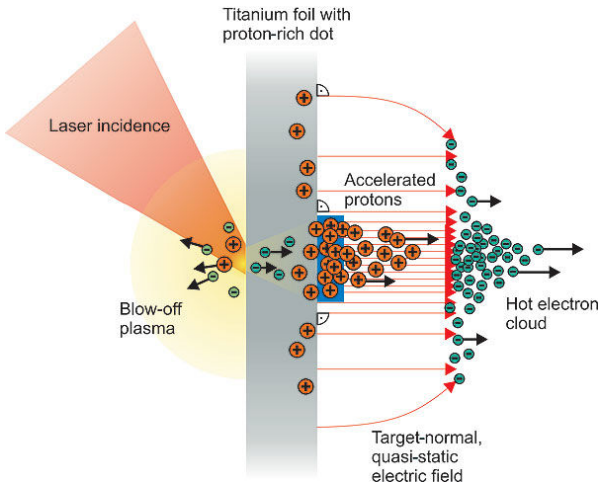

Fig. 1.5. Scheme of the Target Normal Sheath Acceleration [**?**].

Among other ions, protons can be most efficiently accelerated due to their high charge-to-mass ratio. The highest published TNSA proton energy so far is 85 MeV [1].

1.3.2 Radiation Pressure Acceleration (RPA)

Electromagnetic waves carry momentum, since photons, despite being zero-rest mass particles, have nonzero momentum while traveling with the speed of light. So, any surface irradiated by EM wave is exposed to radiation pressure, i.e. the flow of the momentum per unit surface. Radiation pressure P for a plane monochromatic EM wave of intensity I normally incident on the plane surface of a medium at rest can be expressed as [25]

$$P = (1 + R - T)\frac{I}{c} = (2R + A)\frac{I}{c}, \tag{1.17}$$

where R, T and A are the coefficients of reflection, transmission and absorption.

Esirkepov was first to showed that for laser intensities exceeding 10^{23} W/cm^2 radiation pressure acceleration (RPA) becomes the dominant mechanism of ion acceleration instead of the TNSA mechanism [26]. Such intensities are nor yet achieved, but they will be available in the upcoming, next-generation laser facilities (ELI Beamlines [7], ELI-NP (Nuclear Physics) [27], the APOLLON project[28]). Nevertheless, later research [29] have shown, that RPA is also possible for lower intensities (10^{19} W/cm^2), if circular polarization of laser light combined with normal incidence on the target are used.

In this case hot electron generation is strongly suppressed, resulting in the elimination of the TNSA acceleration and the maximization of the radiation pressure.

The concept of RPA is the following. When a laser pulse impinges the overdense plasma, electrons from the plasma surface are pushed inwards by the ponderomotive force, creating a charge separation field. This electrostatic field affects ions and later accelerates them in the forward direction layer-by-layer. Finally, the target ions are set into ballistical motion due to the electrical field generated by the displaced and compressed electron layer which acts as an accelerated plasma mirror. Theoretical background of this regime can be found in [30].

Depending on the target thickness, two further scenarios can take place [25], [23]. Firstly, if the laser propagates through the foil only until limited depth and does not interact with the target rear side, the target is referred to as the thick one. That leads to the acceleration of a part of the target ions through RPA. This is called the 'hole boring' regime. Secondly, in the case when the foil is nm thickness, all ions on the laser path are accelerated as it passes through the entire target, and a slab of the plasma is accelerated as a whole. This regime of RPA is termed as the 'Light Sail' regime. Both cases are pictured in Fig.1.6.

For RPA mechanism being successful, the thin foil target has to be a perfectly reflecting, undeformable plane mirror so that it can be boosted by radiation pressure [31].

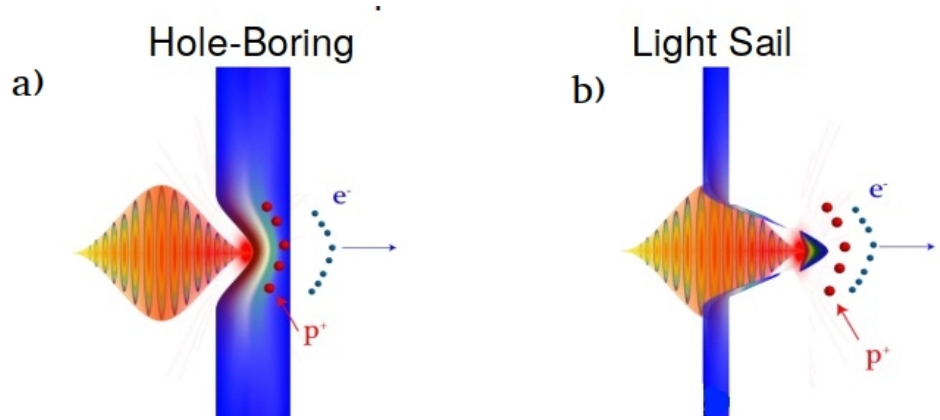

Fig. 1.6. Scheme of the Radiation Pressure Acceleration regimes: a) is the 'Hole Boring' regime and b) is the 'Light Sail' regime. [32].

Chapter 2

Generation of X-rays and γ-rays and their interactions with matter

The electromagnetic spectrum, shown in Fig.2.1, is a continuum of all electromagnetic waves classified according to frequency and wavelength. The region encompassing X-rays and γ-rays acts differently from the rest of the spectrum, as it is characterized by very short wavelengths (and correspondingly high energies). Unlike common 'light', this type of radiation does not reflect from surfaces and shows high penetration power, as due to its short wavelength the probability of interaction with the matter (nucleus or electron) is fairly low. It is is more appropriate to use corpuscular description in the regime of X and γ-rays, in which a photon is characterized by int energy $E = \hbar\omega$.

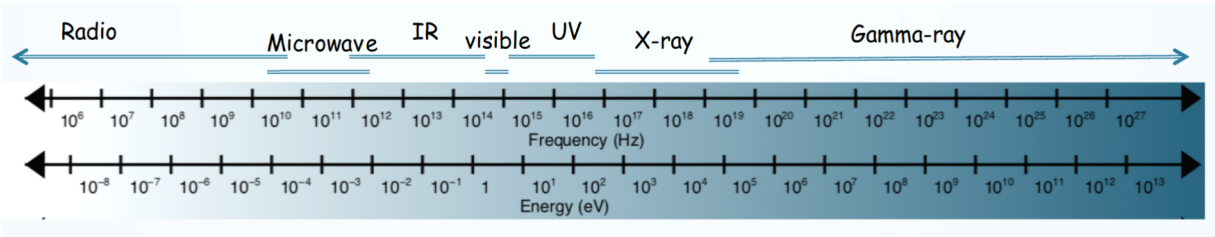

Fig. 2.1. The spectrum of electromagnetic radiation [33].

X-rays and γ-rays have found applications in many aspects of human endeavor, including science, industry and especially medicine. They are best known for their ability to enable imaging through opaque materials and radiation treatment of internal organs. Furthermore, they enable to sterilize medical instruments, kill harmful bacteria and examine metal details for industrial purposes [34]. In particle physics, detection of emitted gamma and X-rays from material can provide particular information (energy, space distribution) about the particles that produced them.

2.1 Classification of ionizing photon radiation from laser plasmas

Once the laser-plasma interaction has happened, the thermal energy of the plasma increases and radiation is emitted in various forms. Usually, it is classified into two

main categories, namely non-ionizing and ionizing radiation. The latter one, in its turn, can be divided into directly (electrons, protons, α-particles and heavy ions) and indirectly ionizing radiation (photons ad neutrons) [35].

Energy deposition of directly ionizing radiation happens through direct Coulomb interactions between the impinging ionizing charged particle and orbital electrons of atoms in the medium. On the contrary, indirectly ionizing radiation deposits energy in the medium through a two step process:

1. a charged particle is released in the medium (photons release electrons or positrons)
2. the released charged particles deposit energy to the medium similarly as in the case of directly ionizing radiation (through direct Coulomb interactions) [36].

Ionizing photon radiation from plasmas generally consists of bremsstrahlung (continuous) X-rays, characteristic X-rays and γ-rays.

Bremsstrahlung X-rays

Bremsstrahlung X-rays are produced when fast electrons pass through a medium. This kind of radiation is caused by inelastic Coulomb interactions between an incident light energetic charged particle and the nucleus of the target material. However, only accelerated or decelerated charged particles (apart from moving with a constant velocity ones) are capable of producing this type of X-rays. The point is, that during such a motion, the non-static electric and magnetic fields of a charged particle can not adjust themselves so that no energy is radiated away. Therefore, decelerating in the field of a nucleus, charged particles lose part of their kinetic energy in the form of bremsstrahlung photons. A scheme of this process is sketched in Fig. 2.2.

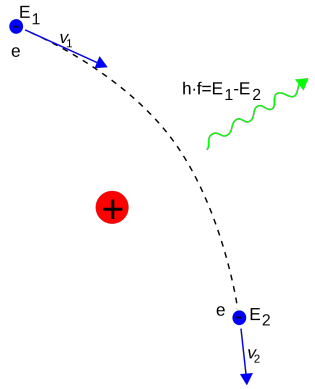

Fig. 2.2. Bremsstrahlung X-rays generated due to electron declaration in the field of a nucleus [37].

Because of their relatively small mass, light charged particles, such as electrons and positrons, are capable of generation of a significant amount of bremsstrahlung photons, while that of heavy charged particles (protons, deuterons, alpha particles and heavier ions) is negligible. Thus, a proton, having relative mass three orders of magnitude greater than that of an electron, will produce much less bremsstrahlung radiation than does an electron, according to Eq. 2.1, $\approx 4 \times 10^6$ times less. The radiation stopping power for electrons in comparison to that for protons is over six orders of magnitude larger at the same velocity and in the same absorbing material. As a result, heavier charged particles lose energy mainly through collision losses, instead of radiation ones. On the other hand, electrons experience both types of losses by interactions with orbital electrons as well as with nucleus of the medium.

The following equation (referred to as Larmor's formula) shows that the power P (energy per unit time) emitted in the form of bremsstrahlung radiation by an accelerated

charged particle is proportional to the square of particle's charge q^2 and the square of particle's acceleration a^2, which is in turn in inverse proportion to the particle's mass [35]:

$$P = \frac{\mathrm{d}E}{\mathrm{d}t} = \frac{1}{6\pi\epsilon}\frac{q^2a^2}{c^3}; \qquad a = \frac{zZe^2}{m}. \tag{2.1}$$

The energy of emitted bremsstrahlung photons ranges from zero up to the maximum kinetic energy of the incident electron, resulting in a continuous bremsstrahlung spectrum (Fig. 2.3). As can be seen from the figure, the emission of low-energy photons usually dominates and towards the electron kinetic energy maximum the spectrum drops sharply to zero. Since bremsstrahlung spectra are in continuous form, they can not be employed for energy calibration of radiation detectors. The spectral intensity of this radiation is proportional to atomic number of the absorbing material [38].

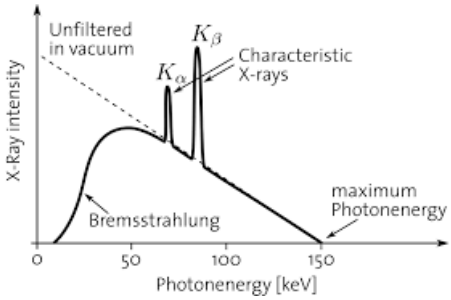

Fig. 2.3. Continuous bremsstrahlung spectrum with characteristic lines. [37].

Characteristic X-rays

In addition to bremsstrahlung radiation, characteristic X-rays are also produced during the electron-matter interaction. They result from transitions of bound electrons in atoms triggered by vacancies in inner electronic shells of the atom.

Vacancies in atomic shells appear due to the orbital electrons disruption from their normal configuration induced by some excitation process (excitation by radioactive decay or external radiation). An atom with a vacancy remains in an excited state for a short period of time and subsequently returns to its ground state through one or several electron transitions. During these transitions, an electron from a higher level atomic shell fills the orbital vacancy and the energy difference between the initial and the final shell is emitted either in the form of characteristic radiation or radiation-less, being transferred to an orbital electron that is afterwards ejected from the atom as an Auger or Coster–Kronig electron [39]. The sketch of characteristic radiation production is shown in Fig. 2.4.

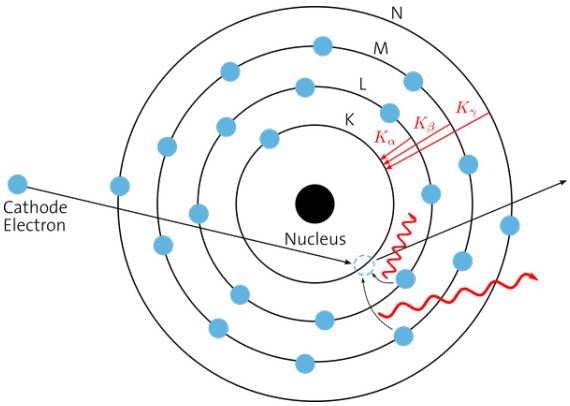

Fig. 2.4. Characteristic X-rays produced by electron transitions between atomic shells [37].

The radiation in this process is referred to as characteristic, since the emitted photons have certain discrete energies $\hbar\omega$ and wavelengths λ that are characteristic of the particular atom from which the photons are originated. The set of characteristic photons emitted from a given atom is called the line spectrum of the atom.

γ rays

There is no explicit boundary between X-rays and γ-rays radiation, though photons carrying kinetic energies exceed-

ing 100 keV are usually called gamma photons [40]. Moreover, gamma radiation is often considered to result rather from nuclear processes than from electron-atom interactions, generating less-energetic X-rays [39].

However, all elementary particles participating somehow in electromagnetic interaction may become sources of γ-rays production. In general, several processes that may lead to γ-radiation can be distinguished. They are illustrated in Fig.2.5) and described below:

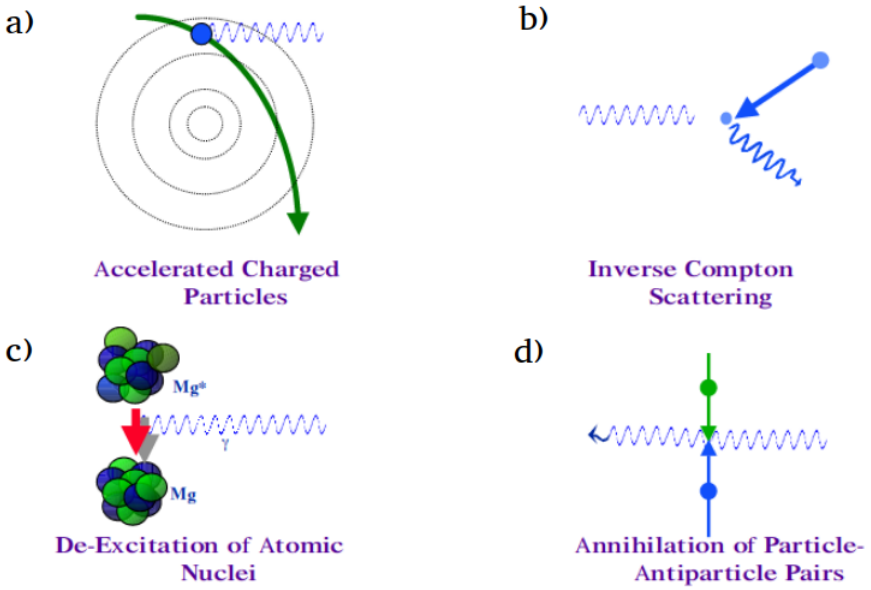

Fig. 2.5. Processes leading to γ-rays production [41].

(a) The acceleration or deceleration of a charged particle of high energy in the force field - bremsstrahlung emission (see above). High energy here points to energies far beyond 1 MeV. If the energy level is low, ion–electron bremsstrahlung dominates over electron–electron bremsstrahlung, while with increasing energy ratio of both becomes balanced.

(b) Colliding with energetic particles, e.g. electrons, lower-energy photons can gain energy during the collisions, thereby getting promoted in energy, i.a. from X-rays to γ-rays. This process is significant in regions of high photon densities and is called 'Inverse-Compton Scattering'.

(c) Gamma radiation during the process of an atomic de-excitation is emitted as a result of transitions of excited nuclei to lower nuclear levels. Excited nuclei are usually created in the α decay as well as three β decay process of a parent radionuclide. Energy of emitted γ-ray photons equals to the difference in energy between the initial and final nuclear states. Because energies of nuclear states and hence emitted γ-rays are well-defined and unique for particular nuclear specie, some specific γ-ray sources are useful in the precise energy calibration of gamma-ray detectors.

(d) Annihilation of particle-antiparticle pairs also cause γ-rays emission. The lightest particle–antiparticle pair that can emerge from pair production process (see 2.2.3) is electron-positron one; creation of such a pair requires a minimum energy of 1.022 MeV. "Annihilation" refers to phenomenon that occurs when a particle encounters its antiparticle, and the mass of both participants is radiated away in the form of two or more (according to conservation laws) photons with energies distributed up to the maximum of 0.511 MeV (for two-photon annihilation).

In laser-plasma interactions, bremsstrahlung emission of γ-rays prevails.

2.2 Passage of photons through matter

Penetrating through the matter, photons may experience a large number of various interaction with the material atoms; the probability of the cross-section for each interaction mechanism depends on the energy of the impinging photon $\hbar\omega$ and the atomic number Z of the absorbing material. These interactions involve either the nuclei of the absorbing material (*photodisintegration, pair production*) or its orbital electrons, that, in turn, can be divided into tightly bound electrons (*photoelectric effect, Rayleigh scattering*) and essentially free orbital electrons (*Thomson scattering, Compton effect, triplet production*). In the context of photon interactions, a tightly bound electron is considered as an orbital electron whose binding energy E_B is comparable to, or larger than the photon energy. Thus, an interaction of a photon with such an electron can occur if $\hbar\omega \geq E_B$ and is treated as an interaction between a photon and the atom as a whole. On the contrast, the binding energy of the "free" orbital electron (or loosely bound electron) is much smaller in comparison with photon energy, i.e. $E_B \ll \hbar\omega$.

After the interaction with an atom the photon may completely disappear (its energy is fully absorbed and transferred to light charged particles) or it may be scattered either coherently (with no change in the photon energy) or incoherently (with the resulting scattered photon having a lower energy than the incident one). The light charged particles produced during the interaction will either deposit their kinetic energy into the medium via Coulomb collisions or radiate it away, as discussed previously.

Although diverse interaction mechanisms are possible, only three of them are crucial in radiation measurements (esp. of X-rays and γ-rays): photoelectric absorption, Compton scattering, and pair production. The photoelectric process dominates at low energies of photons (up to several hundred keV), with the increase in energy Compton scattering starts to prevail and for high-energy photons (above 5-10 MeV) pair production becomes the most probable photon-matter interaction mechanism. In the following text, these mechanisms will be briefly described. More details (along with the description of the remaining mechanisms) are introduced here [35] and here [42].

2.2.1 Photoelectric absorption

The photoelectric absorption is the dominant process for gamma rays (or X-rays) of low energy. During this mechanism a photon undergoes an interaction with a tightly bound orbital electron of the atom that results in a complete absorption of the impinging photon. At the same time, the orbital electron is ejected from one of the atom's bound

shells carrying kinetic energy $E_K = \hbar\omega - E_B$, where E_B represents the binding energy of the photoelectron in its original shell. The most probable origin of the photoelectron for γ and X-rays of sufficient energy is K-shell of the atom, as the most tightly bound electron has the highest probability for interaction with the incident photon.

The photoelectric interaction can happen only with bound electrons, as it includes the atom as a whole: after the interaction occurred, the absorber atom is in an ionized state with a vacancy in one of its shells. The vacancy is filled with an electron from another orbit or through capture of a free electron from the vicinity of the atom and the energy of the electronic transition is emitted away either in the form of one or more characteristic X-rays or in the form of an Auger electron.

The photoelectric interaction between a photon of energy $\hbar\omega$ and a K-shell atomic electron is shown schematically in Fig. 2.6.

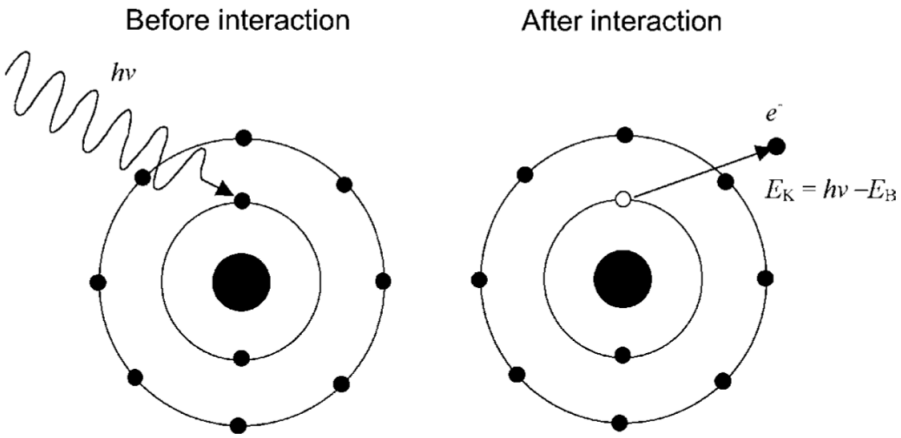

Fig. 2.6. Schematic diagram of the photoelectric effect. [35].

No complete theoretical background for this phenomenon is yet achieved, but a rough approximation of its probability, i.e. photoeffect cross-section, based on numerical fit is the following [43]:

$$\sigma_{ph}(E_\gamma) \propto \frac{Z^4}{E_\gamma^3}, \tag{2.2}$$

where E_γ is a photon energy. As can be seen, the photoeffect cross-section is enhanced for absorber materials of high atomic number and it depressed for incoming photons of high energy. This approximation is useful for the regime where the photoelectric effect is dominant.

2.2.2 Compton scattering

Incoherent scattering of a photon on an essentially free (loosely bound) orbital electron is called Compton scattering. The incident photon energy in this case is much greater than the binding energy of the orbital electron. In this process, an incoming photon strikes the electron (assumed to be initially at rest) and transfers it of its kinetic energy E_K, setting the electron into motion: it is ejected from the atom as a recoil (Compton)

electron. Simultaneously, a scattered photon with energy $\hbar\nu' = \hbar\omega - E_K$ is produced, deflected through a scattering angle θ with respect to the direction of the original photon, as shown schematically in Fig. 2.7. It ranges from $\theta = 0°$ (forward scattering) through 90° (side scattering) to $\theta = 180°$ (back scattering). Since all angles of photon scattering are possible, the energy transfered to the recoil electron may vary between zero and a large portion of the photon energy.

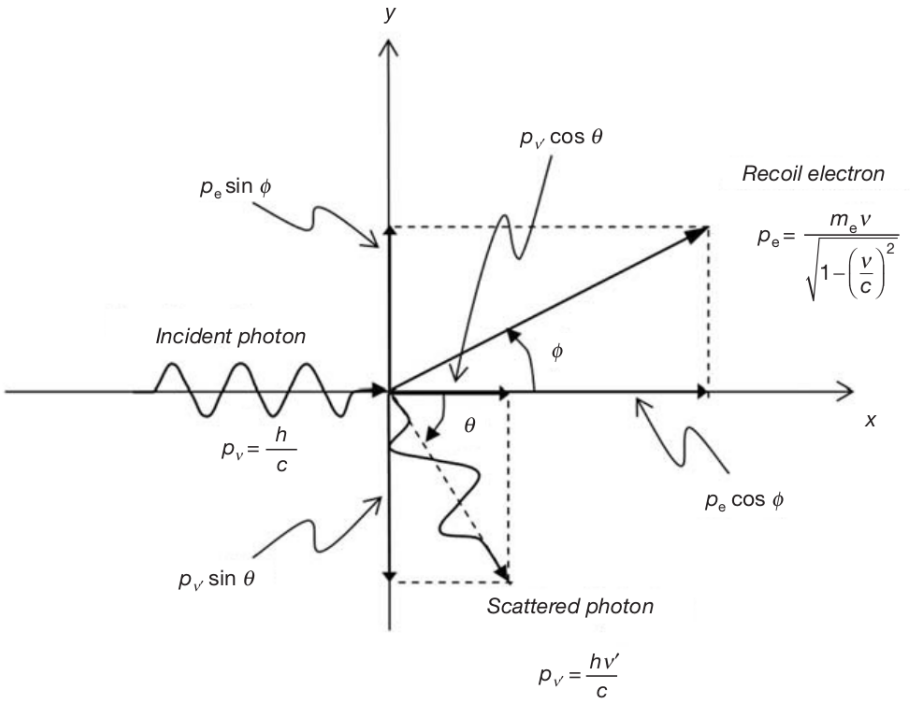

Fig. 2.7. Schematic diagram of Compton scattering . [36].

In the extreme when scattering angle $\theta = \pi$, the energy transfered to electron reaches its maximum for a single Compton interaction. At this energy, the distribution of recoil electrons demonstrates the cut down.

The angular distribution of scattered photons is predicted by Klein-Nishina formula for the differential scattering cross-section (see [39]). and is presented in Fig 2.8. A strong tendency for forward scattering for high-energetic photons is noticeable from the figure.

Compton scattering is most probable for photons in the "medium" energy range (from several hundreds keV to several MeV). Cross-section depends on the number of electrons in the absorber medium available for the interaction and hence increases linearly with the atomic number Z. On the other hand, the probability of this process decreases with increasing energy of photons. Additionally, the it is also limited at low values of energy (< 100 keV), as orbital electrons are bound too tightly to get liberated by the incident photon.

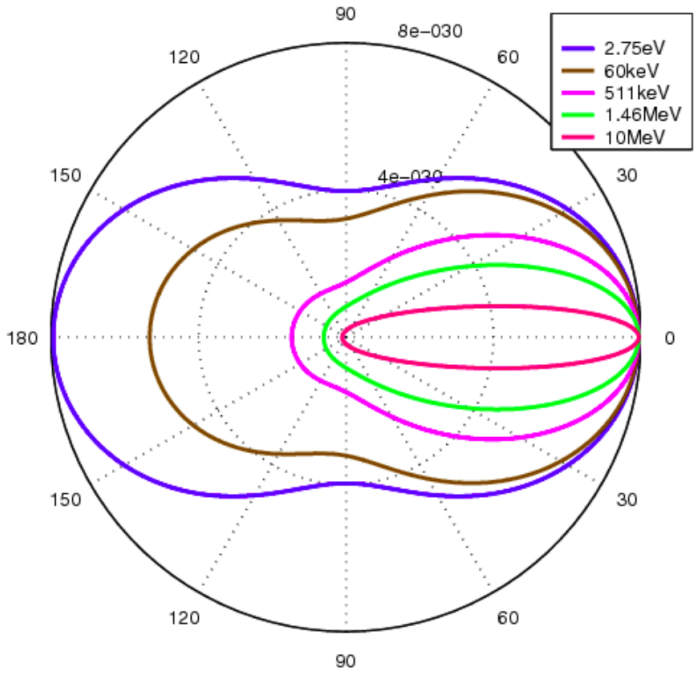

Fig. 2.8. Klein–Nishina distribution of scattering-angle cross sections over a range of commonly encountered energies. [44].

2.2.3 Pair production

The principle of a pair production mechanism is a complete disappearance of the incoming photon leading to subsequent emergence of an electron-positron pair in the nuclear Coulomb field (see Fig. 2.9). A third body, which is usually a nucleus, is required to participate in this interaction so as to conserve energy and momentum of a system. Since both electron and positron are characterized with well-known mass, pair production has an energy threshold of $2m_ec^2 = 1.02$ MeV, which is twice the rest mass of an electron. Thus, only photons with energies exceeding the required minimum will cause this effect to happen.

No simple expression exists for the cross-section of pair production process, but it is proportional to the square of the absorber atomic number and increases rapidly with the photon energy above threshold [35]:

$$\sigma_{pp} \propto Z^2 P(\epsilon, Z), \qquad (2.3)$$

where $P(\epsilon, Z)$ is a function of the photon energy and atomic number of the absorber. As it follows from the equation, materials with higher atomic num-

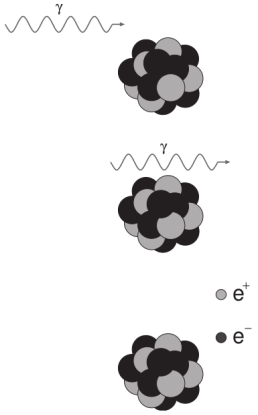

Fig. 2.9. An incoming photon interacts with the Coulomb field of a nucleus. As a result, an electron-positron pair emerges. [42].

bers more readily convert photons into light charged particles in comparison to low atomic number mateails. Additionally, unlike the Compton and photoeffect cross section, the pair production cross section increases with increased photon energy. The relative predominance of the three processes is schematically illustrated in Fig. 2.10 The lines on the scheme correspond to regions where bordering effects are equally probable.

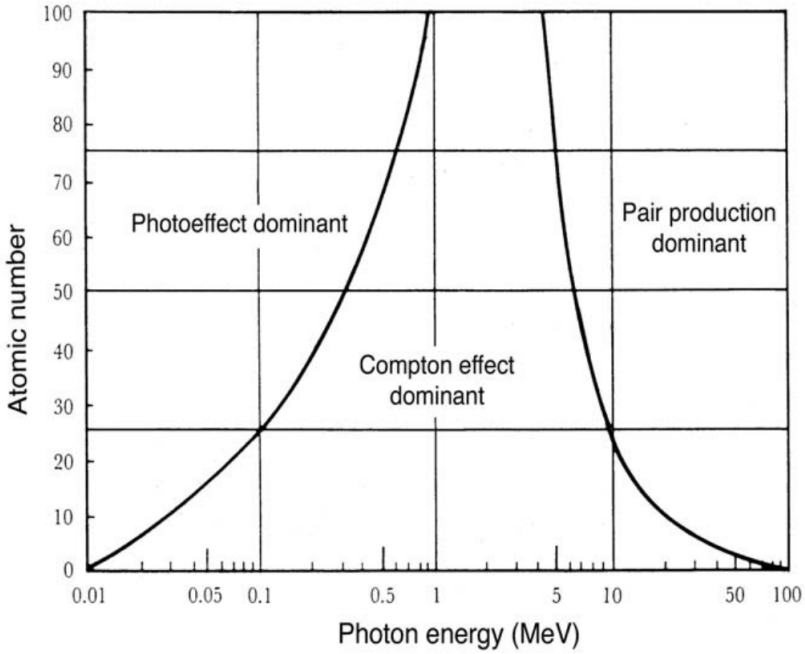

Fig. 2.10. Regions of relative predominance of the three main mechanisms of photon interaction with matter. [36].

Sometimes one of the orbital electrons of the atom act like the necessary third body for pair production mechanism. This effect is called "triplet production", as it results in three particles (two electrons and a positron) leaving the interaction site. In comparison to nuclear pair production, the cross-section is suppressed by a factor of $1/Z$ in this case.

2.2.4 Electromagnetic cascades in matter

Interaction of high-energetic photons or electrons with matter may entail a process called an electromagnetic cascade, in which original high energy of incident particles is converted into multiple amount of lower energy electromagnetic particles propagating through the medium. As was discussed above, at high energies photon interactions consist mainly in materialization in the Coulomb field of a nucleus, giving rise to electron-positron pairs, and in production of recoil Compton electrons. High energetic electrons and positrons, in their turn, undergo bremsstrahlung interaction, which predominates for high energy ranges, leading to production of more photons. These photons may generate further electrons and positrons, provided that their energy is still sufficiently large, and so on. Because of such a spreading and multiplicative nature, this process is

often referred to as an electromagnetic shower. A sketch of the process is presented in Fig. 2.11. Electromagnetic shower is always initiated by an electron or a photon and the generated particles includes only electrons, positrons and photons. The extent of the process is dictated by the magnitude of the incident-particle energy.

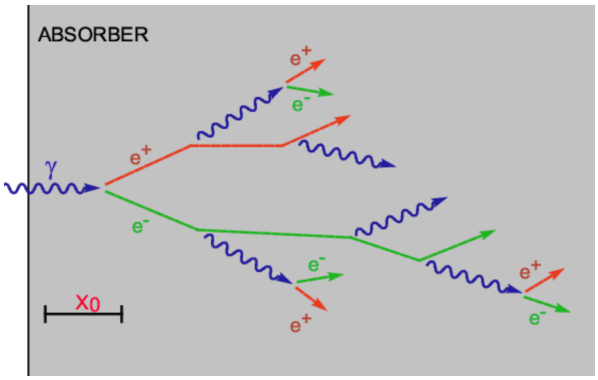

Fig. 2.11. A schematic description of electromagnetic shower development principle. [45].

Typically, shower's expansion exhibits cone-like shape, with the vertex represented by the initially incident particle. As the original particle's energy increases, the penetration depth grows as well , while the opening angle of the cone rather decreases, given that particles of high energy are deflected less in matter.

The energy below which particles within the cascade no longer engenders further particles is termed the critical energy ϵ_c. After such a threshold, photons transfer remaining energy to the medium via the photoelectric process, while electrons dissipate it through collisions with other particles. In this manner, the incident energy is absorbed by the medium. Special detectors constructed to measure the energy deposited in their volume from such an energy degradation are called electromagnetic calorimeters.

The characteristic quantities described in the following text are essential for understanding of electromagnetic cascades. In the shower process, the energy is propagated both laterally and longitudinally within the material. Longitudinal development is governed by so called radiation length X_0, while lateral shower width scales with Molière radius R_M:

- *the radiation length* represents the mean free-path distance of an electron in a material traveled while radiative processes occur and is denoted by X_0 (in units of cm) or by X_{g0} (in units of g/cm^2). The latter definition appears to be convenient when different modifications of detector proportions and/or absorbing materials are taken into account.

  Over this distance the electron has typically reduced its energy by a factor e. Additionally, the radiation length constitutes 7/9 of the average distance that high-energetic photon has to travel before its materialization. This quantity is a material constant, depending on the atomic number Z, mass number A and density of absorber ρ, commonly approximated by [46]:

$$X_0 \approx \frac{A}{\rho Z^2} \quad [\text{cm}]. \tag{2.4}$$

- *The Molière radius* characterizes the cascade lateral-spread caused by several physical processes. Since the cascade development results in production of low-energy electrons that dissipate their energy mainly through collisions, processes as Compton scattering and photoeffect are taken into consideration. In this processes, secondary electrons are generated which directions of motion no longer coincide with incoming-photon directions and can be even emitted backwards. Scattered sideways, such low-energy electrons induce further collisional interactions that eventually lead to the spread of electron directions that differ from the initial axis defined by original particle.

  The Molière radius is in fact a radius of a cylinder around the original track of the particle, comprising nearly 90% of the energy deposited in electromagnetic shower. It is defined as [42]:

$$R_M = \left(\frac{E_s}{\epsilon_c}\right) X_0 \quad [\text{cm}], \tag{2.5}$$

  where E_s= 21.2 MeV is the scale energy combined of universal constant, ϵ_c is the critical energy and X_0 os the radiation length.

  For rapid estimates, it is also possible to use the following relation [46]:

$$R_M = \frac{7A}{Z}. \tag{2.6}$$

- As it was mentioned above, *the critical energy* ϵ_c is an approximation of the energy at which electron's radiation losses via bremsstrahlung become equal to collisional losses via excitation and ionization. That indicates that below this value of energy, charged particles no longer contribute to the development of the electromagnetic cascade. One of the approximation formulas for the critical energy is given by [42]:

$$\epsilon_c = B\left(\frac{ZX_0g}{A}\right)^h \quad [\text{MeV}], \tag{2.7}$$

  where A is a mass number of the absorber, X_0g is the radiation length in g/cm^2, $B = 2.66$ and $h = 1.11$.

Quantitative values of described quantities for some absorbers used for calorimeters are presented in Table 2.1.

Material	X_0 [cm]	R_M [cm]	E_c [MeV]
Al	8.89	4.68	40.28
BGO	1.12	2.33	10.20
Pb	0.56	1.60	7.42
U	0.32	1.00	6.77
Water	36.08	10.91	70.10

Table 2.1: Values of the radiation length X_0 using Eq. 2.4, Molière radius R_M using Eq. 2.5 and critical energy E_c using Eq. 2.7 [42].

Chapter 3

Diagnostics for measuring gamma and X-ray radiation

In order to choose the configuration of a detector that is being developed for gamma and X-rays detection in upcoming experiments of ELIMAIA group from ELI Beamlines facility, various commonly used photon diagnostics were studied. There are several interaction media that gamma and X-rays detectors are normally based on. This chapter includes brief description of such materials and gives an overview of widely used detectors.

3.1 Main design

3.1.1 Gas-filled detectors

A gas-filled detector is basically a metal chamber with a sensitive volume filled with a gas (such as Ar or He) situated between two electrodes. In most designs, the cylindrical wall of the gas pressure vessel acts like the outer electrode, while the inner one (positively biased anode) is represented by a thin wire located in the center of the chamber. Voltage is applied between the two electrodes, producing an electric field in the detecting volume. When photons pass through the chamber, they ionize the gas through secondary electrons , leading to creation of free electrons and positive ions. The electrons are attracted to the anode wire, where they are collected and the electric pulse is recorded. Depending on the magnitude of applied voltage, design, filling gas, etc., several types of gas-filled detectors are employed.

At relatively low voltages ($\approx 200-400$ V - [47]), produced electron-ion pairs do not have enough energy to cause any secondary ionization and only primary electrons are collected. This type of detector is called an *ionization chamber*. At higher voltages ($\approx 400-800$ V), primary electrons can attain enough energy to cause further ionizations during their acceleration toward the anode. This detector is known as a *proportional counter*. With further increase in applied voltage, the electron multiplication process in the gas becomes even greater until it reaches saturation and the number of collected electrons becomes independent of the initial energy deposited in the gas. This type of detector is known as the *Geiger-Mueller (GM) detector*.

An ionization chamber and the GM counter provide an accurate overall dose reading,

but not allowing to differentiate among incoming particles or measure their energy spectrum. A proportional counter can provide energy resolution for gamma and X-rays with energy only of a few tens of keV, as only low-energy photons can interact efficiently in the gas (see [48] for instance).

3.1.2 Semiconductor detectors

Solid-state detectors generally consist of semiconductor materials. In many applications, as measurement of high-energy gamma rays, the use of a solid detection medium appears to be highly beneficial, as detector dimensions can be much smaller than the equivalent gas-filled detector (due to higher density).

Semiconductors are materials that can behave as a conductor or insulator depending on the energy of inner electrons. A feature that determine the way the semiconductor will act as, is a band gap. Energy gap or band gap of a semiconductor is in fact energy required to turn a valence electron bound to the atom into a conduction electron.Usually, the band gap is in the range 1 - 5 eV [39]. Typically, main composition parts of semiconductor detectors are active region, constituted by intrinsic or low-doped (with introduced impurities) semiconductor, and junctions located at two sides of the semiconductor. When impinging particles interact with the detector active layer, they can induce a production of electron-holes pairs, provided that their energy is large enough to overcome the band gap. Reversed bias applied on junctions induces generation of the electric field that forces the electrons and the holes to drift towards electrodes. A current is detected by the electrode, integrated by a charge sensitive preamplifier and converted to a voltage pulse. The output voltage is proportional to the radiation energy.

The most common and efficient semiconductor materials by far are Silicon and Germanium with band gaps 1.12 eV and 0.74 eV respectively. Silicon predominates in the diode detectors used mostly for charged particles measurements, while Germanium is more widely used in the gamma-ray detection, having higher atomic number [49].

Besides being much more compact in comparison to gas-filled detectors, semiconductor detectors provide a much better energy resolution, since only a small amount of energy is required to produce an electron-hole pair(3.61 eV for Si, 2.98 eV for Ge). Additionally, semiconductor devices are characterized by relatively fast time response (due to the high speed of charge carriers). Drawbacks include the need for cooling to decrease the dark current noise of the detector and signal degradation from radiation-induced damages in their structure.

3.1.3 Passive detectors

Passive detectors employ so called imaging plates to measure incident radiation. Imaging plates are made of photostimulable phosphor applied onto a polyester film and are able to record an image of the radiation through phosphor excitation.

Typically, in such detectors imaging plates alternate with absorbing medium (usually high-Z material), enabling to measure energy and spatial distribution of the incident radiation(e.g. [50]).

Passive detectors are commonly used for diagnostics as they are EMP (electromagnetic pulse) resistant. However,they are unable to work in real-time. After the interac-

tion image plates have to be removed from the detector for subsequent time-demanding post-processing, making high-repletion regime impossible.

3.1.4 Scintillators

In high-energy gamma-rays measurements, a large area of detectors incorporates scintillation materials. Basically, a scintillator is a luminescent material that emits light when it absorbs radiation, instead of its direct conversion into electric charge as described in 3.1.1 and 3.1.2. The light pulse is subsequently converted into electrical signal by a light detector. To be successfully employed in photon detection, a scintillation material should possess certain properties, such as i) easily detectable emitted light with a high scintillation efficiency, ii) the light yield proportional to deposited energy (linear conversion), iii) transparency of a scintillation crystal to the wavelength of its own emission, iv) short time decay of the induced luminescence (enabling fast signals generation), v) firm enough to be manufactured in sufficiently large sizes and to remain in good optical quality and vi) index of refraction suitable for scintillator coupling to PMT or other light detector . However, no scintillator known so far can satisfy all the requirements simultaneously. Despite hundreds of scintillation materials are already available nowadays, the research in this field is still ongoing, aiming to discover an ideal scintillator [51], [52].

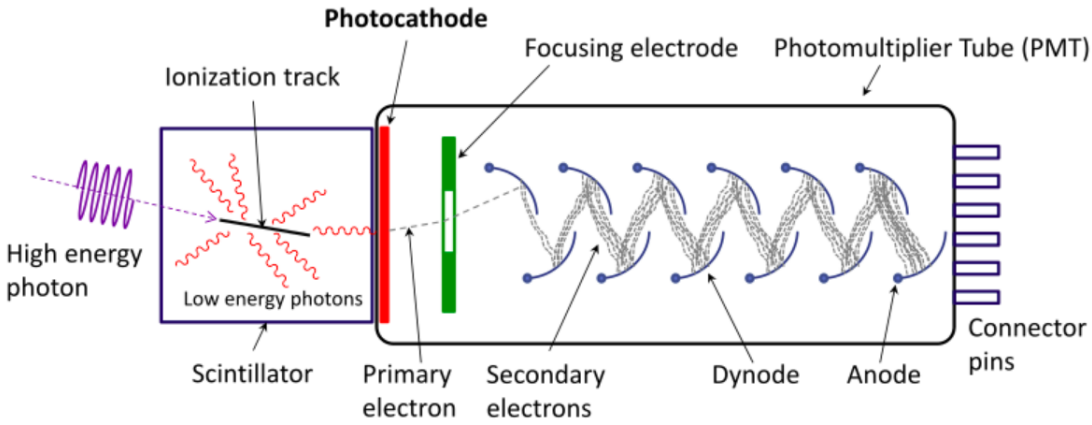

Fig. 3.1. Schematic of high energy photon hitting a scintillator material and inducing the release of low-energy photons which are then converted into photoelectrons subjected to further multiplication in photomultiplier tube [53].

A schematic view of a scintillator coupled to a PM tube is shown in Fig 3.1. When a high-energy photon hits a scintillator material, its energy is converted to energetic electrons via one of the processes described in Chapter 2, and atoms get ionized along the photon track. During the following atomic de-excitation in the scintillator, a burst of low energy photons is emitted. To convert the outputted light into electrical signal, a light detector can be coupled to the scintillation crystal via light guides. The most frequently used one is the photomultiplier tube (PMT). As can be seen from the figure, the first element of the PMT facing the incident light is a photocathode. Scintillation photons hitting the photocathode liberate electrons through the photoelectric effect.

Under the impact of an electrical potential, the group of primary electrons is accelerated and focused on the first electrode (called a dynode) in the tube, releasing more secondary electrons, that are accelerated again to collide with the next dynode and so on. The potential difference between each pair of neighboring dynodes is higher than the previous one, enabling further acceleration and finally leading to a large multiplication of the electron flux from its initial value. Usually, the total accelerating voltage is between 500-3000 V [54]. Finally, the resultant output signal at the anode is collected and processed by appropriate electronics. The magnitude of this signal is proportional to the initial amount of electrons emitted by the photocathode.

The scintillation material may be organic or inorganic. The latter is more commonly used for high energy photon detection due to high atomic number (higher density). Small amounts of impurities (called activators) are added to most inorganic scintillators to enhance the emission of visible photons, as atomic de-excitations in this case can be channeled through these impurities and lead to emission of detectable (by PMT) visible light. Good examples of such crystals are commonly used sodium iodide NaI(Tl) and cesium iodide CSI(Tl) scintillator materials which are doped with thallium. However, some inorganic materials that do not require doping: bismuth germanate $Bi_4Ge_3O_{12}$ (commonly referred to as BGO), lead tungstate $PbWO_4$ (PWO). The inorganics are usually characterized with the best light output and linearity, but mostly are relatively slow in their response time.

Organic scintillators are aromatic hydrocarbon compounds containing a benzenic cycle (e.g. anthracene, plastics). During the de-excitation, organic scintillators emit bands of ultraviolet (UV) light which can be absorbed by most organic materials in a few mm length. Hence, to extract the produced light, another fluorescent material called a *wavelength shifter* (WS) should be used, that contributes to conversion of UV into visible light. WSs can also be used for transport of scintillation light to photosensetive device if light has to be collected at a location distant from the scintillator. Organic scintillators are generally faster than inorganic ones, but not linear and have low density and low atomic number and, therefore, yield less light and have relatively low absorption for gamma- and X-rays [39].

Scintillators were chosen to be used in our detector design (see Chap. 4), because they are EMP resistant, active, and in a calorimeter setup (see section 3.2) they can provide spectral information.

3.2 Electromagnetic calorimeters

Calorimeters are detectors designed to measure energy deposited by an incident particle. Such devices can be divided into 2 categories according to the type of the particles of interest: electromagnetic (EM) calorimeters, used to measure mainly electrons and photons trough their electromagnetic interactions (e.g. bremsstrahlung, pair production), and hadronic calorimeters, used to detect mainly hadrons through their strong and electromagnetic interactions. In this work the focus is laid on the EM calorimeters (for hadronic ones see [55]).

The energy deposition in these devices occurs through the development of electromagnetic cascades (the physics of this process is discussed in the section on “Passage of Particles Through Matter ”). Therefore, the size of a calorimeter is determined by

the radiation length X_0 (Eq. 2.4) of the shower. Since X_0 increases only logarithmically with energy, the detector length also needs to increase only logarithmically with the energy of incident particles, making calorimeters space and hence cost effective for high-energy measurements.

According to the construction technique, calorimeters can be classified into homogeneous and sampling calorimeters.

3.2.1 Homogeneous calorimeters

In this type of calorimeters, its entire volume is sensitive and contributes signal. This results in excellent energy resolution of such devices, as the primary energy is fully deposited in the active part, in contrast to sampling calorimeters. However, they are not able to accomplish position measurements, since being less easily longitudinally and laterally segmented. Additionally, their cost can be quite high. Homogeneous calorimeters may be made of inorganic heavy scintillators (such as BGO, CsI, NaI, PWO), semiconductors, Cherenkov radiators, or ionizing noble liquids [56]. Schematic of a homogeneous calorimeter is sketched in Fig. 3.2.

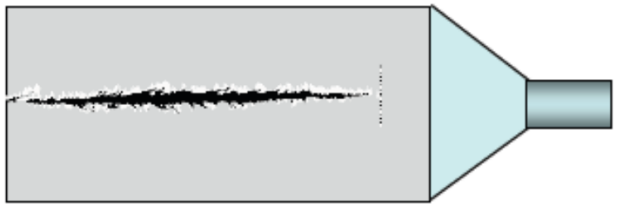

Fig. 3.2. Schematic of a homogeneous calorimeter [57].

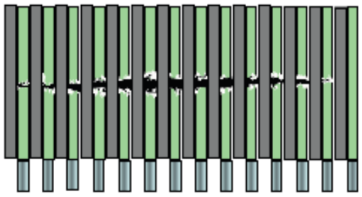

Fig. 3.3. Schematic of a sampling calorimeter [57].

3.2.2 Sampling calorimeters

A sampling calorimeter consists of alternating layers of passive medium (metallic absorber) and active material which generates the signal. The active medium may be a scintillator (both organic and inorganic)), an ionizing noble liquid, a gas chamber, or a semiconductor. The absorber is usually represented by a material og high density (lead, iron, copper). Such a structure implies that the energy resolution is worse than that of homogeneous calorimeters due to fluctuations produced by the absorber layers interleaved with the active layers.On the other hand, sampling calorimeters can be more compact (and cheaper) if high density absorber is chosen. Additionally, they can provide with spatial resolution, since they are easily segmented. The positional resolution depends on the Moilere radius (Eq. 2.5). Schematic of a sampling calorimeter is shown in Fig. 3.3.

3.2.3 Energy resolution

The energy resolution $\sigma(E)/\sqrt{E}$ of a calorimeter can be parametrized as $a/\sqrt{E} \oplus b \oplus c/E$, where $\oplus$ represents addition in quadrature and E is in GeV [55]. The stochastic term

a due to the fluctuations related to the physical development of the shower. For a homogeneous calorimeter the term a is usually at a few percent level, while for sampling calorimeters it is in the range 5-20% [56]. Term b is called a systematic, or constant, term and is affected by the detector non-uniformity, calibration uncertainty and radiation damage of the active medium. This term can be reduced below one percent by developing radiation-hard active media [58] and by regular calibration and monitoring [59]. The term c is due to electronic noise of the readout chain. Some examples of the energy resolution for different calorimeters is presented in Table 3.1.

Material (experiment)	Depth	Energy resolution
CsI (KTeV)	$27X_0$	$2\%/\sqrt{E} \oplus 0.45\%$
PWO (CMS)	$25X_0$	$3\%/\sqrt{E} \oplus 0.5\% \oplus 0.2/E$
Scintillator/Pb (CDF)	$18X_0$	$13.5\%/\sqrt{E}$
Scintillator fiber/Pb (KLOE)	$15X_0$	$5.7\%/\sqrt{E} \oplus 0.6\%$

Table 3.1: Energy resolution of typical electromagnetic calorimeters: first two are homogeneous, last two are sampling. The resolution of latter ones is worse, while their size is smaller in comparison to homogeneous devices [55].

.

Chapter 4

Preliminary design of high-energy photons detector for experiments on laser-driven ion acceleration

In this chapter we summarize the current progress of the high-energy photons detector that is being developed in collaboration between ELIMAIA and Monte Carlo groups from ELI Beamlines laser facility.

Since high-repetition-rate petawatt lasers will be employed during upcoming ELIMAIA experiments (with intensities exceeding 10^{21} W/cm^2), very intense gamma-ray bursts with femtosecond duration will be produced during laser-matter interactions (with temperatures up to 50 MeV) at such laser intensities. The currently available diagnostics are not suitable for spectroscopy of such intense and short photon bursts, therefore there is a need of a new type of a detector. The required detector should satisfy several criteria. The most important ones are the following: first, the detector has to be capable of working in online regime, on shot-to-shot basis, and second, it has to provide quality information about the energy spectrum of the incident gamma-rays. Also, the detector should be relatively compact in order to be portable and cost-effective, and not affected by EMP (electromagnetic pulse) coming from the laser-to-matter interaction.

After the study of most commonly used photon diagnostics (see chap. 3), the choice of the detector fell on the electromagnetic calorimeter type, as such a device meets the required criteria the best.

In that regard, we started a collaboration with the High Energy Density group from the Helmholtz-Zentrum Dresden-Rossendorf, since a prototype of the electromagnetic calorimeter was implemented there recently [60]. The calorimeter designing approach differs from classical calorimeters arrangements. In this case, the device consists of multiple layers of different scintillating materials that serve as absorbers and detectors of the radiation at the same time. Resting on such a design, we have modified the calorimeter as regards types of scintillators employed and the number of layers. Also, an estimation of the photon temperature in the ELIMAIA future experiments was carried out in order to determine the detector's dimensions and composition materials. After that, multiple simulations were performed to test the detector's design, as it is the most economical and fast method of examination.

This chapter starts giving predictions of the anticipated photons energy. This is followed by descriptions of the simulations setup, the unfolding algorithm used and

summaries of the current results.

4.1 Estimation of the photons temperature

Temperatures of the hot electrons and the photons emitted by them are assumed to be in the same range, therefore it is possible to employ formulas known for the hot electrons temperature prediction to estimate that of photons.

Based on experimental data, Beg *et al.* [62] empirically derived that hot electron temperature scales T_h as $(I\lambda^2)^{0.3}$ for laser intensities up to $I\lambda^2 = 10^{18}$ W cm^{-2} :

$$T_h(MeV) = 0.215 \left(\frac{I\lambda^2}{10^{18}\mathrm{Wcm}^{-2}\mu\mathrm{m}^2} \right)^{1/3}. \tag{4.1}$$

Later, it was discovered that even for intensities up to $I\lambda^2 = 8 \times 10^{20}$ W cm^{-2} the effective temperature is in substantial agreement with the Beg scaling [63].

Other recent simulations found that right after the interaction hot electron temperature satisfies [64]:

$$T_h(MeV) = 1.01 \left(\frac{I\lambda^2}{10^{18}\mathrm{Wcm}^{-2}\mu\mathrm{m}^2} \right)^{1/3}. \tag{4.2}$$

which agrees with the Beg scaling, but shows larger coefficient, as the optimized resonant conditions for incident angle and the plasma scale length are considered in this case.

In ELIMAIA experiments, ultrahigh laser intensities up to $10^{22} - 10^{23}$ W cm^{-2} might be achieved. No experimental data are available yet to make any precise predictions of the hot electron temperature for such intensities. However, using the formulas above, we can estimate that it might be in the range (5 ; 22) MeV for the intensity of 10^{22} W cm^{-2}, and (10 ; 47) MeV for 10^{23} W cm^{-2}, where the first number is calculated using Eq. (4.1) and the second one using Eq. (4.2). So, it is possible to conclude that most likely gamma-rays temperature will not exceed 50 MeV.

4.2 Simulations of gamma-ray detector performance

The simulations were performed using the FLUKA Monte Carlo code, which simulate the transport of radiation and its interaction with the matter. It is jointly developed by the European Organization for Nuclear Research (CERN) and the Italian Institute for Nuclear Physics (INFN) [65], [66].

4.2.1 Simulation setup and results

The detector was modeled in 3D using the FLUKA graphical interface Flair [67]. The simulation setup was simplified for the reason of acceleration of the simulation process. The medium surrounding the calorimeter was set as vacuum, which is in compliance with an expected real experimental setup. The photon source is located 20 cm in front of the calorimeter and emits photons in a form of a pencil beam (non-divergent and

point-like) along the calorimeter axis. The photons energy spectrum was set according to the Maxwell-Boltzmann (MB) distribution Eq. (4.3), assuming that the spectrum of the hot electrons, which mainly produce these photons, satisfies the MB distribution.

$$f(E) = 2\sqrt{\frac{E}{\pi}}\left(\frac{1}{kT}\right)^{3/2} e^{-E/kT}, \tag{4.3}$$

where T is the temperature of generated photons, E is the energy and k is the Boltzmann constant. A typical shape of the MB temperature distribution for 50 MeV photon beam is shown in Fig. 4.1.

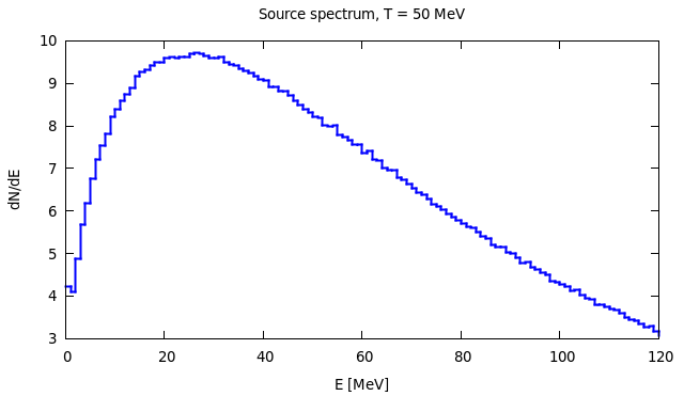

Fig. 4.1. Input photon energy spectrum satisfies Maxwell-Boltzmann distribution with the mean of $T = 50$ MeV.

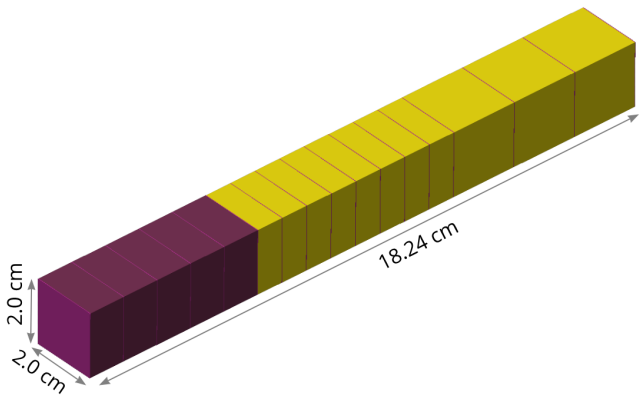

Fig. 4.2. Flair 3D view of the realistic arrangement of the electromagnetic calorimeter. Front layers pictured in violet correspond to plastic layers, while the remaining yellow part corresponds to PWO layers.

Several designs were studied, including more realistic and simplified arrangements.

1. The first one, shown in Fig. 4.2, is based on two scintillating materials - plastic and PWO ($PbWO_4$). The latter one was employed as it is quite commonly used in high-energy physics [68]. The design consists of 5 plastic layers (1.1 cm), 8 thin PWO layers (0.7 cm) and 3 thick PWO layers (2.0 cm), separated from each other by teflon

light insulating layers. The total length of the detector is 18.24 cm, width and height of it equal 2 cm each. Plastic scintillators constitute the front part of the detector in order to resolve the low energy part of incident photons, since their density is low enough (1.03 g/cm^3). The remaining part of the device is made of by PWO scintillators, which cause higher energy deposition due to their high-density (8.23 g/cm^3) and high atomic number. The last PWO layers were designed to be thicker in order to collect more output light, since the signal is getting weaker towards the detector's edge.

For the first arrangement we simulated the interaction with the detector of a photon beam having temperature ranging from 5 MeV to 120 MeV with 1 MeV-step to ascertain with what energy ranges the calorimeter will be able to cope.

Energy deposited by 50 MeV photons within the calorimeter is shown in 1D in Fig. 4.3 and in 2D in Fig. 4.4. It is evident from the figures, that the energy deposition increases dramatically at the border between the plastic and the PWO material and then gradually decreases. It reaches the maximum at the beginning of the PWO layers. Each layer can be easily distinguished in Fig. 4.3 due to a drop of the deposited energy in teflon connectors between them. In Fig. 4.4 the deposited energy in the calorimeter is shown on a logarithmic scale; it can be seen from the plot that the deposition maximum is inside the calorimeter and occurs in thin PWO layers.

Fractions of the energy deposited in several adjacent layers depending on the the simulated temperatures of the photon beam are shown in Fig. 4.5 and Fig. 4.6(logarithmic scale). It is clear from the figures that the largest rise in the deposited energy is between layers 6 and 7; also, the fraction E_7/E_6 increases monotonically and sharply with temperature in comparison to other fractions. It indicates that theoretically we could resolve initial photon temperature distribution using mainly this fraction. In the case of a monoenergetic 50 MeV MB distributed photon beam (see Fig. 4.5), all the measured fractions indeed indicate the correct input temperature value. However, in reality it might not be that easy, as an ideal one-temperature MB distribution is not achievable. Fig. 4.6 confirms it, showing the case when the incident photon temperature is constituted of a sum of 2 MD distributions; every fraction indicates different temperatures making it impossible to identify the input temperature of the photons. Therefore, there is a need of signal unfolding (see sec. 4.3).

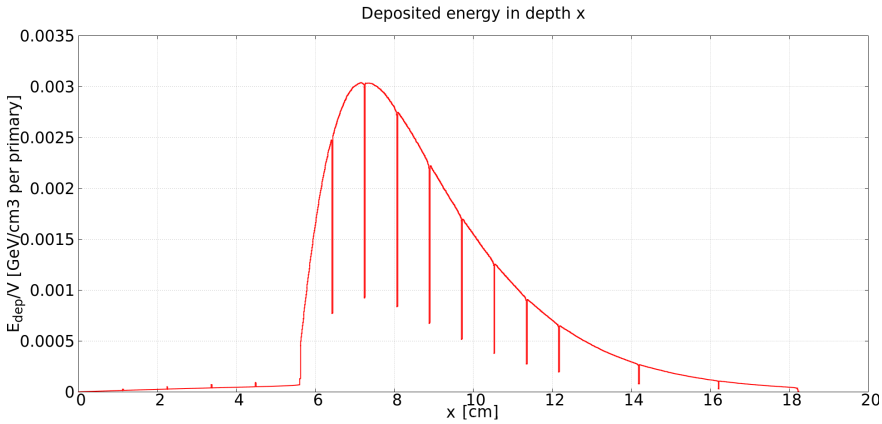

Fig. 4.3. Energy deposited within the multi-layered calorimeter, 1D plot.

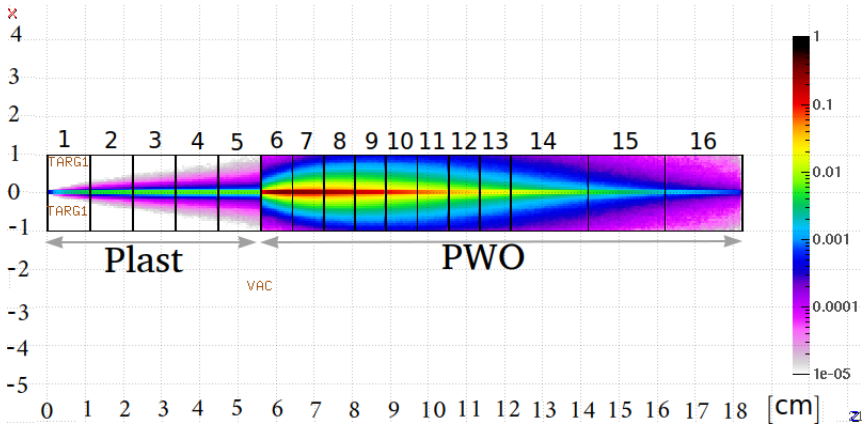

Fig. 4.4. Energy deposited within the multi-layered calorimeter, [GeV/cm^3], 2D plot, logarithmic scale.

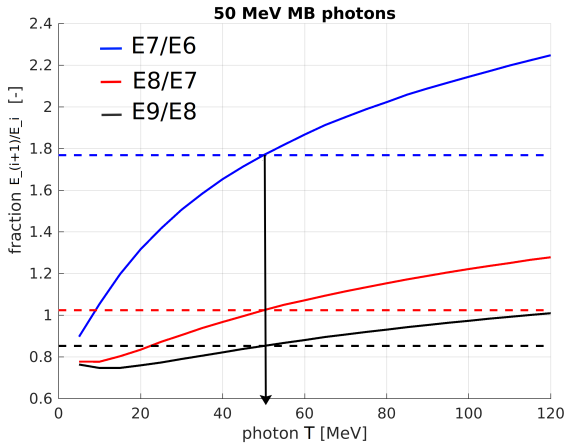

Fig. 4.5. Fractions of the energy deposited by a monochromatic 50 MeV photon beam in central layers of the calorimeter. All the fractions indicate the same temperature of the photon beam.

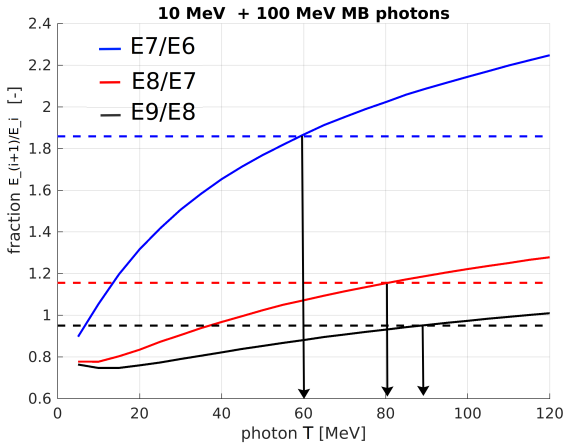

Fig. 4.6. Fractions of the energy deposited by photon beam of two MB temperatures in central layers of the calorimeter. Every fraction indicates different temperatures of the photon beam.

2. After the tests performed with the first arrangement it was realized that the division of the calorimeter into blocks is an unnecessary complication from the point of view of the general study of the materials and the unfolding algorithm. Therefore, the second simplified design was implemented: the detector's dimensions are similar as in the previous case, but it consists of only 2 sections of scintillators; still, the effect of the presence of as many layer as in the previous simulations was taken into account thanks to the binning structure. Plastic was kept as the front-layer material, whereas for the second layer two options were examined: PWO and BGO ($Bi_4Ge_3O_{12}$) dense scintillators. The BGO scintillator was taken into account, because, similar to PWO, it is characterized with a high density (7.13 g/cm^3), but the light yield of this material is almost 100 times larger than that of PWO, which implies better signal.

In this simplified case the range of the tested photon temperatures was reduced to

the maximum of 100 MeV, instead of 120 MeV.

In the arrangement using the PWO dense layer, the energy was deposited similarly as in the previous design, except for the drops caused by teflon. However, when BGO was set as the second layer, the detector showed the anticipated differences in the energy deposition. Comparison between the position of the energy deposition peak in the PWO and the BGO layers depending on the input photon energy for both calorimeters arrangements are presented in Fig. 4.7. As can be seen, when the BGO scintillator is used, the peak moves deeper in the calorimeter with the increasing input temperature, because of its lower density in comparison to PWO.

Moreover, it is evident from the figure that for this energy range the peak of the deposited energy is inside the calorimeter for both arrangements. This fact indicates that there is no need of elongation of the calorimeter and the employed length of 18.24 cm is enough for such measurements.

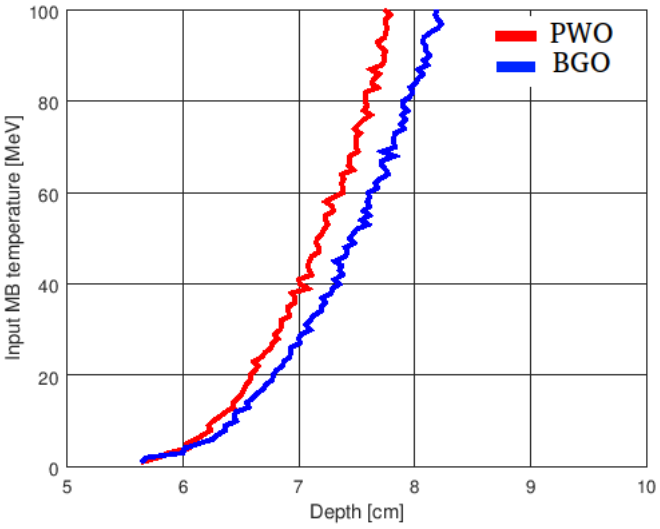

Fig. 4.7. Movement of the energy deposition peak in the calorimeter PWO or BGO layer for input photon temperatures 1 - 100 MeV. Red - PWO, blue - BGO.

4.3 Signal unfolding

In signal processing a reconstruction of some original undistorted physical quantity based on detector's response is called a signal unfolding. The unfolding can be implemented using different methods depending on the detector and the measured quantity.

In our case we need to unfold energy distribution of the incident photon proceeding from the measurement of the energy deposited within the calorimeter. We implemented and tested the following technique:

- Gauss elimination with pivoting

On the basis of the performed simulations it is possible to create a so called *calorimeter response matrix* $E_{m,n}$, where m is a number of points in which energy deposition

was scored along the calorimeters length and n is a number of simulated photon MB distributed temperatures. In our case the response matrix has the following form:

$$E_{m,n} = E_{1824,100} = \begin{pmatrix} e_{1,1} & e_{1,2} & \cdots & e_{1,100} \\ e_{2,1} & e_{2,2} & \cdots & e_{2,100} \\ \vdots & \vdots & \ddots & \vdots \\ e_{1824,1} & e_{1824,2} & \cdots & e_{1824,100} \end{pmatrix}$$

Assuming that $\overrightarrow{D}$ is a signal measured by the calorimeter and $\overrightarrow{X}$ is a ratio of MB distributed temperatures presented in the incident photon beam, it is possible to formulate the unfolding problem as a search of the solution of the following system of linear equations:

$$E_{m,n} \cdot \overrightarrow{X} = \overrightarrow{D}. \tag{4.4}$$

The solution, i.e. the vector $\overrightarrow{X}$, can be found by Gauss elimination algorithm with pivoting (for instance, using Matlab software).

To understand if the introduced method is correct, we solved the Eq.(4.4) using a test vector $\overrightarrow{D}$ set as $\overrightarrow{D} = 5\overrightarrow{E}_{20} + 7\overrightarrow{E}_{40} + 2\overrightarrow{E}_{60}$, which is a combination of three MB temperatures with different ratios. The solution vector $\overrightarrow{X}$, representing the ratio of the MB distributions in the incident photon beam, depending on the prescribed calorimeter response, is shown in Fig. 4.8. The x-axis depicts all the temperatures presented in the response matrix and the y-axis indicates if any of these temperatures were presented in the incident photon beam and their corresponding weight.

An ideal case is shown on the left, with no noise added to the calorimeter response (vector $\overrightarrow{D}$). As can be seen, the unfolding algorithm evaluated the input temperatures and their ratios correctly in this case, showing three distinctive peaks of different height.

The right plot depicts the solution vector in the case when small noise was included to the calorimeter response vector $\overrightarrow{D}$ by addition of a random number to every vector element (signal-to-noise ratio is 10^{-4}). As it can be seen, the unfolding algorithm becomes no longer reliable. Although the added noise is very small, deviations are significant and it is difficult to distinguish the peaks. In reality, the signal-to-noise ratio of the detector is expected to be much higher than the mentioned value (due to the detector fluctuations, electronic noise, etc..). However, with the further increase of the added noise, the implemented algorithm becomes not able to cope with the unfolding.

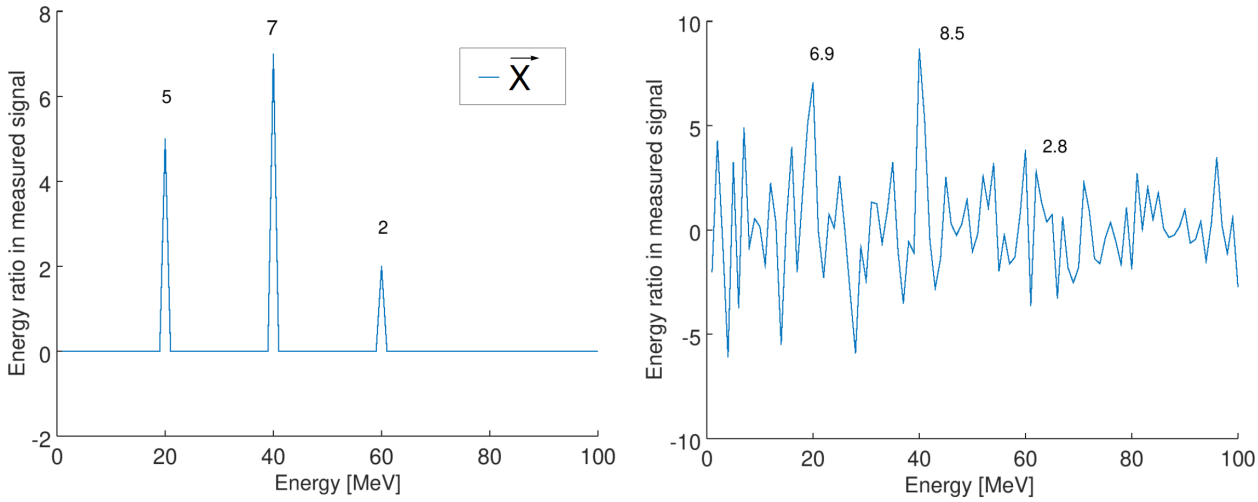

Fig. 4.8. Unfolding of a calorimeters signal after its interaction with a photon beam combined of 3 MB functions: left - without noise; right - with small noise.

4.3.1 Discussions

Performed temperature estimations for photons emitted by hot electrons have shown that the upper limit of the photons temperature will probably not exceed 50 MeV. Therefore, the future calorimeter has to be able to detect photons with temperatures up to this temperature. According to the simulations, the calorimeter's length of 18.24 cm is completely enough for this purpose, as during the interaction with 50 MeV photons it keeps the peak of the deposited energy inside. This makes it a quite compact device, which is very effective from the practical point of view; theoretically such a detector can be inserted even inside the target chamber close to the interaction area.

From the distribution of the deposited energy inside the detector (Fig. 4.4) we may conclude that the maximum energy is deposited during the first couple of cm of PWO, so it is reasonable to have as many layers in this region as possible to obtain better energy resolution. However, there are some connected issues. The first one is that the amount of layers is constrained by the the minimum layer thickness achievable to manufacture (down to 30 μm [69]). The second one is that the thiner the layer, the less light it can produce. Therefore, a compromise between thickness and efficiency should be found.

The comparison of the peak movement inside the two-sections calorimeter with the PWO and the BGO parts indicates that if BGO is used as the second calorimeter layer, the detector will become longer, granting more space for energy deposition, and hence easier to manufacture. Additionally, BGO possesses more than 100 times higher light yield (see Table 4.1), improving light detection and enabling the employment of thin scintillator layers.

So, we can conclude that the BGO scintillator is probably optimal for our case, in comparison to the PWO one. However, study of other possible materials is ongoing. Essential parameters of BGO, PWO and other potential materials are presented in the table below. High light yield implies better signal and high density enables to detect photons of high energy within small distances.

Scintilator	Density [g/cm^3]	Light Yield [#/MeV]
BGO	7.13	8 000
CsI	4.51	41 000
LuAG:Ce	6.73	25 000
PWO	8.23	100
YAG:Ce	4.57	30 000
YAP:Ce	5.37	25 000

Table 4.1: Possible materials for the dense region of the calorimeter.

The unfolding technique based on the Gauss elimination algorithm appears to work correctly under ideal conditions, when no noise is added to the response of the detector. However, in more realistic situations the algorithm collapses, even if the amount of noise contained is very small. The reason is that the system of equations is underdetermined (fewer equations than unknowns). Nevertheless, studies of other suitable algorithms are in progress.

Another thing that should be further studied is an input photon beam shape and divergence. During the simulation the incoming beam had a pencil shape, which is not consistent with real experiments.

Other remaining issues to be solved for the realization of a working detector are: the EMP (electromagnetic pulse), which can be potentially solved by transporting of the light signal to processing electronics via long light guides or wave-length shifters; separation photon emission incident on the detector from other plasma emitted particles (ions, electrons..).

Conclusion

The main goal of the thesis is to develop a novel type of diagnostics for measuring high-energy photon radiation from laser-plasma interactions that is intended to be used in the future experiments of the ELIMAIA project at ELI-Beamlines. Such a device should be capable to estimate the temperature of the generated photons. The progresses that have been achieved so far are summarized in this work.

After search in literature for possible photon detectors, an electromagnetic calorimeter based on scintillating materials was chosen, as it is capable of working in online regime, has compact size and apart from the energy distribution can also provide a spatial one. Low density plastic scintillators for were chosen to detect low photon energies, while for higher photon energies (PWO_4) and BGO ($Bi_4Ge_3O_{12}$) materials were employed due to their high density.

Estimations of the photon temperature were made; according to these estimations, the temperature will not exceed 50 MeV. Consequently, simulations were performed using the Monte Carlo FLUKA code to test different arrangements of the detector during the interaction with the photons of a broad range of temperatures. The calorimeter length of 18.24 cm appeared to be sufficient for the detection of expected radiation.

The BGO scintillator was deemed more appropriate than PWO to be used for the denser layers of the calorimeter, as it produces more light while being almost as dense as PWO. Several configurations, in terms of materials and crystal thickness are being investigated.

The unfolding algorithm based on the Gauss elimination principle was implemented and tested. Although it showed a correct evaluation of the original photon energy from the detector response, it collapsed when the noise was added to the prescribed detector signal. The search for unfolding algorithm capable of giving reliable results under experimental conditions is still ongoing.

In addition to already mentioned effort, plans for the future include improvement of the calorimeter design (number of materials used, number of layers..), simulations with more realistic input beam (square shape, divergence..), solving the problem of the EMP impact on electronics. The final goal of this research is to manufacture the electromagnetic calorimeter and to test it in real experiments.

Bibliography

[1] F. Wagner, et.al. Maximum Proton Energy above 85 MeV from the Relativistic Interaction of Laser Pulses with Micrometer Thick CH_2 Targets. *Physical Review Letters*, 115(20):205002, 2016.

[2] T. H. Maiman. Stimulated optical radiation in ruby. *Nature*, 187, pp. 493-494, 1960.

[3] T. Tajima, J. M. Dawson. Laser electron accelerator, *Physical Review Letters* 43, pp. 267–270 (1979).

[4] Michael D. Perry, Gerard A. Mourou. Terawatt to Petawatt Subpicosecond Lasers, *Science*, 264, pp. 917–924, 1994.

[5] Gerard A. Mourou. Optics in the relativistic regime, *Reviews of Modern Physics*, 78(2), pp. 309–371, 2006.

[6] Peter Mulser and Dieter Bauer. *High power laser-matter interaction*, volume 238. Springer Science & Business Media, 2010.

[7] ELI Beamlines official website, `eli-beams.eu`, accessed on 31.7.18.

[8] F.F. Chen. *Introduction to plasma physics*, 2nd edition, Plenum Press, New York (1984).

[9] A. Otto, Transparencies of lectures on Magnetospheric Physics, Chapter 2, 2006. Online at `http://how.gi.alaska.edu/ao/msp/chapters/chapter2.pdf`, accessed on 1.8.2018.

[10] B. Sedlák, I. Štoll. *Elektřina a magentismus*, Charles University in Prague, Karolinum Press, 2017.

[11] A. Henig. *Advanced Approaches to High Intensity Laser-Driven Ion Acceleration.* Dissertation thesis, Ludwig Maximilians University in Munich, Germany, 2010.

[12] Jan Pšikal. *Ion Acceleration in Small-size Targets by Ultra-intense Short Laser Pulses (Simulation and Theory).* PhD thesis, Czech Technical University in Prague, Czech Republic, 2009.

[13] H. Daido, M. Nishiuchi, A.S. Pirozhkov. Review of laser-driven ion sources and their applications. *Reports on Progress in Physics*, 75(5):056401, 2012.

[14] J. F. Seely. Quantum Theory of Inverse Bremsstrahlung Absorption and Pair Production. *Laser interaction and related plasma phenomena*, Springer, Boston, MA, pp. 835-847, 1974.

[15] Matthew M. Allen. *Ion Acceleration from the Interaction of Ultra-Intense Lasers with Solid Foils*. PhD thesis,University of California, Berkeley, 2004.

[16] S. Atzeni, J. Meyer-Ter-Vehn. The physics of inertial fusion, Clarendon Press, Oxford, pp. 371–389, 2004.

[17] F. Brunel. Not-so-resonant, resonant absorption. *Physical Review Letters*, 59(1):52, 1987.

[18] Jan Kaufman, *Development of Radiochromic Film Diagnostics for Laser-Driven ion beams*. Master thesis, Czech Technical University in Prague, Czech Republic, 2015.

[19] K. W. D. Ledingham and W. Galster. Laser-driven particle and photon beams and some applications. *New Journal of Physics*, 12(4):045005, 2010.

[20] D. B. Zou, et.al. Laser-Driven Ion Acceleration from Plasma Micro-Channel Targets. *Scientific Reports*, 7:42666, 2017.

[21] D. Margarone, et. al. ELIMAIA: A Laser-Driven Ion Accelerator for Multidisciplinary Applications, *Quantum Beam Science*, 2(2): 8, 2018.

[22] B. M. Hegelich, et.al. Laser acceleration of quasi-monoenergetic MeV ion beams. *Nature*, 439(7075), pp. 441-444, 2006.

[23] A. P. L. Robinson, et.al. Relativistically correct hole-boring and ion acceleration by circularly polarized laser pulses. *Plasma Physics and Controlled Fusion*, 51(2):024004, 2009.

[24] S. C. Wilks, et.al. Energetic proton generation in ultra-intense laser-solid interactions. *Physics of Plasmas*, 8:542, 2001.

[25] A. Macchi, M. Borghesi and M. Passoni. Ion acceleration by superintense laser-plasma interaction. *Reviews of Modern Physics*, 85(2): 751, 2013.

[26] T. Esirkepov, et.al. Highly Efficient Relativistic-Ion Generation in the Laser-Piston Regime. *Physical Review Letters*, 92(17):175003 (2004)

[27] ELI-NP official website, `http://www.eli-np.ro/`, accessed on 25.8.2018.

[28] D. N. Papadopoulos, et al. The Apollon 10 PW laser: experimental and theoretical investigation of the temporal characteristics. *High Power Laser Science and Engineering*, 4, 2016.

[29] A. Macchi, et.al. Laser Acceleration of Ion Bunches at the Front Surface of Overdense Plasmas. *Physical Review Letters*, 94(16), 165003 (2005).

[30] S. Steinke. *Ion Acceleration in the Laser Transparency Regime*, PhD thesis, Mathematik und Naturwissenschaften - der Technischen Universität Berlin, Berlin, 2010.

[31] A. Macchi, et.al. Radiation Pressure Acceleration of Ultrathin Foils. *New Journal of Physics*, 12(4):045013, 2010.

[32] Paul McKenna. *Laser-driven ion acceleration from ultrathin foil targets*. Available online at `https://www.cockcroft.ac.uk/wp-content/uploads/2016/06/McKenna_Cockcroft-talk_w.pdf`, accessed 20.06.2017.

[33] Elizabeth Ferrara's presentation for IAC Winter School, Gamma-ray mechanisms, sources and signatures, 2015. online at `http://www.iac.es/winterschool/2015/media/lectures/Ferrara_lecture1.pdf`

[34] A. Mohammadbagher, Advantages of gamma radiation in science and industry. *Journal of Advanced Physics*, 3, pp. 1-7, 2014.

[35] E. B. Podgorsak, *Radiation Physics for Medical Physicists*. Berlin: Springer, 2006.

[36] E.B. Podgorsak, *Radiation oncology physics: a handbook for teachers and students*. Chaper 1, Vienna: International Atomic Energy Agency, pp. 123-271, 2005.

[37] Prof. Dr. P. Cattin, Transparencies of lectures on Principles of Medical Imaging, 2016. `https://miac.unibas.ch/PMI/pdf/PMI-01-BasicsOfXray.pdf` accessed on 1.8.2018.

[38] D. Giulietti, L. A. Gizzi, X-Ray Emission from Laser Produced Plasmas, *La Rivista del Nuovo Cimento (1978-1999)*, 21(10), pp. 1-93, 1998.

[39] G. F. Knoll, *Radiation Detection and Measurement*. 4th edition, John Wiley & Sons, 2010.

[40] A. Richards. *Alien vision: exploring the electromagnetic spectrum with imaging technology*, Vol. 9, Bellingham and Washington, DC: SPIE press, 2001.

[41] Diehl R. Gamma-Ray Production and Absorption Processes, In *The Universe in Gamma Rays,*, Springer, Berlin, Heidelberg, pp. 9-25, 2011.

[42] C. Leroy C, P.G. Rancoita. *Principles of radiation interaction in matter and detection*. World Scientific, 2nd edition, 2009.

[43] A. F. Bielajew. *Fundamentals of the Monte Carlo method for neutral and charged particle transport*. The University of Michigan, 2001.

[44] Klein–Nishina formula, Wikipedia, online at `https://en.wikipedia.org/wiki/Klein%E2%80%93Nishina_formula`, accessed on 23.08.2018.

[45] A. Segreto, *et.al.*, Cosmic rays tracks on the PICsIT detector. *Astronomy & Astrophysics*, 411(1), pp. L215-L222, 2003.

[46] U. Amaldi. Fluctuations in calorimetry measurements. *Physica Scripta*, 23(4A), 409, 1981.

[47] Radiation detectors, DOE Fundamentals Handbook, Instrumentation And Control, vol.2, U.S. Department of Energy, Washington, D.C. , 1992.

[48] M.S. Hemn, M.H. Ari, ^{54} Xe and ^{36}Kr Gas Filled Proportional Counters and Characteristic X-rays Detection, *American Journal of Physics and Applications*, 2(4), pp. 95-103, 2014.

[49] P. N. Luke, M. Amman, C. Tindall, J.S. Lee . Recent developments in semiconductor gamma-ray detectors. *Journal of radioanalytical and nuclear chemistry*, 264(1), pp. 145-153, 2005.

[50] C. D. Chen, et al. Bremsstrahlung and K_a fluorescence measurements for inferring conversion efficiencies into fast ignition relevant hot electrons, *Physics of Plasmas*, 16(8): 082705, 2009.

[51] F. Camera, A. Giaz. New scintillator materials for future and present facilities, *AIP Conference Proceedings*, 1645 (1), pp.253-258, 2015.

[52] P. Lecoq, M. Korzhik. New inorganic scintillation materials development for medical imaging, *IEEE Transactions on Nuclear Science*, 49(4), pp. 1651-1654, 2002.

[53] Scintillation counter, Wikipedia, online at `https://en.wikipedia.org/wiki/Scintillation_counter`, accessed on 25.8.2018.

[54] KK Hamamatsu Photonics. *Photomultiplier tubes: Basics and applications*. 3d edition, Chapter 5, 2006.

[55] K. A. Olive and Particle Data Group. Review of particle physics, *Chinese Physics C*, 38(9): 090001, 2014.

[56] C. W. Fabjan and F. Gianotti. Calorimetry for particle physics. *Reviews of Modern Physics*, 75(4): 1243, 2003.

[57] Presentation of Prof. Karl Jakobs, Albert-Ludwigs-Universität Freiburg. Energy measurement in calorimeters, available at: `http://www.particles.uni-freiburg.de/dateien/vorlesungsdateien/particledetectors/kap8`, accessed on 15.9.2018.

[58] G. Gratta, et.al. Crystal calorimeters in particle physics. *Annual Review of Nuclear and Particle Science*, 44(1), pp. 453-500, 1994.

[59] R. Y. Zhu. Radiation damage in scintillating crystals. *Nuclear Instruments and Methods in Physics Research Section A: Accelerators, Spectrometers, Detectors and Associated Equipment*, 413(2-3), pp. 297-311, 1998.

[60] M. Molodtsova. Development of a novel active technique for bremsstrahlung source term determination in laser-plasma experiments. Poster presented at: 13th Meeting of the task-force on Shielding aspects of Accelerators, Targets and Irradiation Facilities; 2016 Oct 12-16; Dresden, Germany.

[61] P. Gibbon. *Short pulse laser interactions with matter: An introduction*, Imperial College Press, London, UK, 2005.

[62] Beg, F. N et al,. A study of picosecond laser–solid interactions up to 10^{19} W cm^{-2}. *Physics of plasmas*, 4(2), pp 447-457, 1997.

[63] H. Chen et al., Hot electron energy distributions from ultraintense laser solid interactions. *Physics of plasmas*, 16(2): 020705, 2009.

[64] Y. Q. Cui et al., Laser absorption and hot electron temperature scalings in laser–plasma interactions. *Plasma Physics and Controlled Fusion*, 55(8): 085008, 2013.

[65] A. Ferrari, et al. FLUKA: A multi-particle transport code (Program version 2005). No. INFN-TC-05-11, 2005.

[66] G. Battistoni, et al. The FLUKA code: Description and benchmarking, *AIP Conference proceedings*, 896(1), 2007.

[67] V.Vlachoudis. FLAIR: A Powerful But User Friendly Graphical Interface For FLUKA. *Proc. Int. Conf. on Mathematics, Computational Methods & Reactor Physics (M&C 2009), Saratoga Springs, New York*, 2009.

[68] M.J. Kim, *et al.*, Characterization of PbWO4 crystals for high-energy physics experiments, *Journal of the Korean Physical Society*, 69(6), pp. 1130-1134, 2016.

[69] MARKETECH International Inc, official website, online at: `https://mkt-intl.com/materials/single-crystals-optical-materials/scintillator-crystals/`, accessed on 15.9.2018.